Available online at www.sciencedirect.com
SCIENCE DIRECT®
Precambrian Research 147 (2006) 260–278
Precambrian Research
www.elsevier.com/locate/precamres

# Mafic intrusions in southwestern Siberia and implications for a Neoproterozoic connection with Laurentia

D.P. Gladkochub [a], M.T.D. Wingate [b,*], S.A. Pisarevsky [b], T.V. Donskaya [a], A.M. Mazukabzov [a], V.A. Ponomarchuk [c], A.M. Stanevich [a]

[a] *Institute of the Earth's Crust, Siberian Branch, Russian Academy of Sciences, Lermontova Avenue 128, 664033 Irkutsk, Russia*
[b] *Tectonics Special Research Centre, School of Earth and Geographical Sciences, The University of Western Australia, 35 Stirling Highway, Crawley, WA 6009, Australia*
[c] *United Institute of Geology, Geophysics, and Mineralogy, Siberian Branch, Russian Academy of Sciences, Koptyug Avenue 3, 630090 Novosibirsk, Russia*

Received 25 January 2005; received in revised form 4 May 2005; accepted 6 January 2006

**Abstract**

Geochemical and geochronological studies reveal three distinct groups of Neoproterozoic to Early Paleozoic mafic intrusions in the Biryusa metamorphic massif of southwestern Siberia. Group 1 includes mafic sills that intruded Neoproterozoic passive-margin sediments, and were sourced from mantle-derived melts contaminated by crustal components. One sill yielded a plagioclase $^{40}Ar$–$^{39}Ar$ age of $741 \pm 4$ Ma, similar to ages of sills in the adjacent Sharyzhalgai metamorphic massif (all ages are $\pm 2\sigma$ or 95%). Group 2 is represented by north-trending dolerite dykes, one of which furnished a $^{40}Ar$–$^{39}Ar$ age of $612 \pm 6$ Ma. Group 2 dykes may have formed by passive asthenospheric upwelling and decompression during lithospheric stretching within the Neoproterozoic passive margin, a suggestion supported by the occurrence of coeval carbonatites and alkaline ultramafic rocks in the adjacent Sharyzhalgai massif. Group 3 consists of NW-trending dolerite dykes produced by melting of a lithospheric mantle source metasomatised by subduction-related fluids. Zircons from one Group 3 dyke provided a SHRIMP U–Pb zircon age of $511 \pm 5$ Ma, similar to the age of regional metamorphism during Early Paleozoic orogenesis. Our results show that mafic intrusions, broadly similar in age to the Franklin intrusions of northern Laurentia, exist along the southwestern margin of Siberia. Paleomagnetic data permit a reconstruction in which southern Siberia is located opposite northern Canada, but at a sufficient distance to accommodate other crustal blocks (e.g. northern Alaska, Chukchi Peninsula), and in which Group 1 intrusions could be distal products of the mid-Neoproterozoic Franklin mantle plume that affected northern Laurentia.


*Keywords:* Geochemistry; Geochronology; Mafic intrusion; Laurentia; Neoproterozoic; Rodinia; Siberia

## 1. Introduction

The Precambrian tectonic history of Siberia has been debated extensively in recent years, and much discussion has focused on the role of the Siberian craton in the assembly and breakup of the Late Meso-to-Neoproterozoic supercontinent Rodinia, and on Siberia's movements during Neoproterozoic and Late Paleozoic time (e.g. Frost et al., 1998; Smethurst et al., 1998; Ernst et al., 2000; Kheraskova et al., 2003; Pisarevsky et al., 2000, 2003; Pisarevsky and Natapov, 2003, and references therein). Most Rodinia reconstructions place Siberia north of Laurentia (present coordinates), but in a variety of relative orientations. A reconstruction in which

* Corresponding author.
*E-mail address:* mwingate@tsrc.uwa.edu.au (M.T.D. Wingate).

0301-9268/$ – see front matter © 2006 Elsevier B.V. All rights reserved.
doi:10.1016/j.precamres.2006.01.018

the northern and eastern margins of Siberia are juxtaposed against western Laurentia and northern Australia, respectively, was advocated by Sears and Price (2003) and Sears et al. (2004).

Comparison of Late Proterozoic mafic rocks in southern Siberia with those in Laurentia and Australia can provide tests of these reconstructions. There are two giant radiating dyke swarms in northern Laurentia that are apparently truncated at the northern margin of the continent: the 1267 Ma Mackenzie swarm and the 723 Ma Franklin swarm (Fahrig, 1987; Ernst and Buchan, 2001). Widespread mafic magmatism occurred in the southwest US at 1100–1070 Ma (Ernst and Buchan, 2001, and references therein) and along the western Laurentian margin at 780 Ma (Gunbarrel event, Harlan et al., 2003). Significant Late Proterozoic mafic magmatic events in Australia include the 1075 Ma Warakurna Large Igneous Province (Wingate et al., 2004), 825 Ma Gairdner dykes (Wingate et al., 1998), 755 Ma Mundine Well dykes (Wingate and Giddings, 2000), and the 511 Ma Kalkarinji Large Igneous Province (Hanley and Wingate, 2000; Glass, 2002). If Siberia was adjacent to Laurentia or Australia, or both, during the Meso- or Neoproterozoic, its margins might be expected to contain some trace of these huge magmatic events. Finding equivalents in Siberia of mafic events in Laurentia or Australia, or both, would provide compelling evidence that the continents were in close proximity during Late Proterozoic time.

The southwestern margin of Siberia is an ideal place to look for such evidence, because Precambrian basement rocks (Biryusa and Sharyzhalgai massifs, Fig. 1) along this margin are overlain by Neoproterozoic sedimentary successions (Karagas Group) interpreted to have formed at a passive margin, and intruded by an abundance of mafic rocks (e.g. Sklyarov et al., 2001, 2003; Pisarevsky and Natapov, 2003). This study was undertaken to better understand the tectonic history of the southwestern margin of Siberia, by obtaining precise U–Pb and $^{40}Ar$–$^{39}Ar$ ages for mafic intrusions in the Biryusa massif, by classifying these intrusions geochemically, and by constraining the age of the Karagas Group sedimentary rocks.

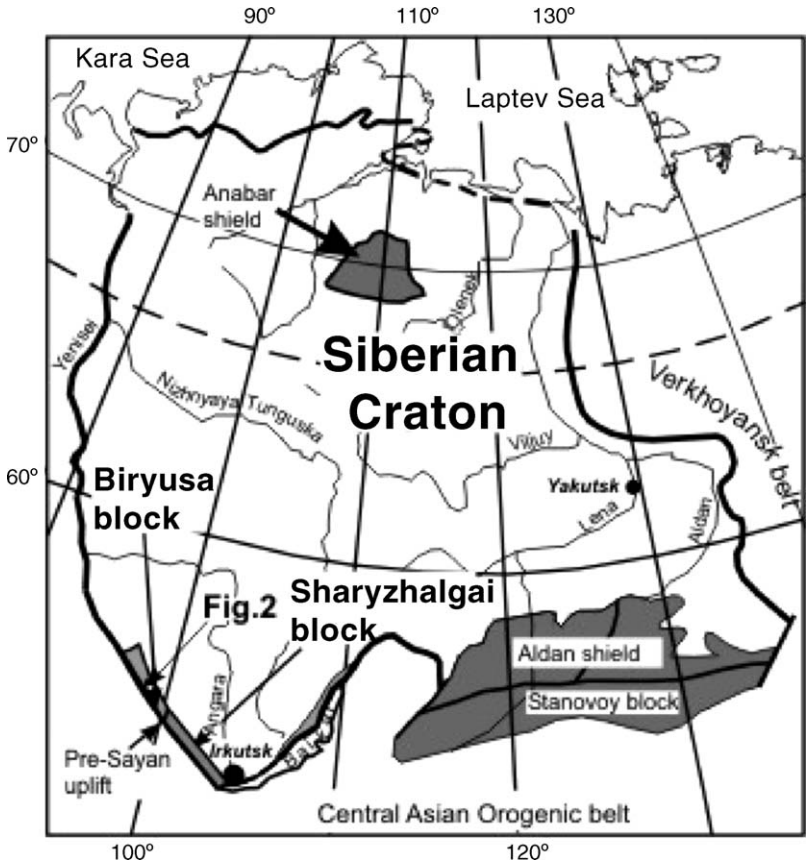


Fig. 1. Map of the Siberian craton showing major basement blocks and location of the study area (Biryusa block).

## 2. Regional geology

Archean to Paleoproterozoic metamorphic and magmatic crystalline basement complexes (Levitskii et al., 2002; Turkina et al., 2003) are exposed inboard of the northwest-trending, dextral strike-slip Main Sayan fault which separates the southwestern margin of the Siberian craton from the Phanerozoic East Sayan fold belt (Fig. 1). Basement rocks of the Biryusa massif (the area of this study, Fig. 2) are overlain by the c. 3.7 km thick Karagas Group, a succession of Neoproterozoic sub-greenschist grade sedimentary rocks interpreted to have formed at a passive continental margin (Sklyarov et al., 2001). The lower and middle Karagas Group contains coarse sandstone, arkose, and conglomerate intercalated with volcanic rocks, is intruded by mafic sills (Fig. 2), and may represent the rift stage of continental breakup. The upper Karagas Group contains turbidites and siliciclastic and carbonate sediments (Sklyarov et al., 2001). The unconformably overlying Late Neoproterozoic Oselkovaya Group contains mainly clastic marine sediments with carbonates and turbidites in its upper part, although its

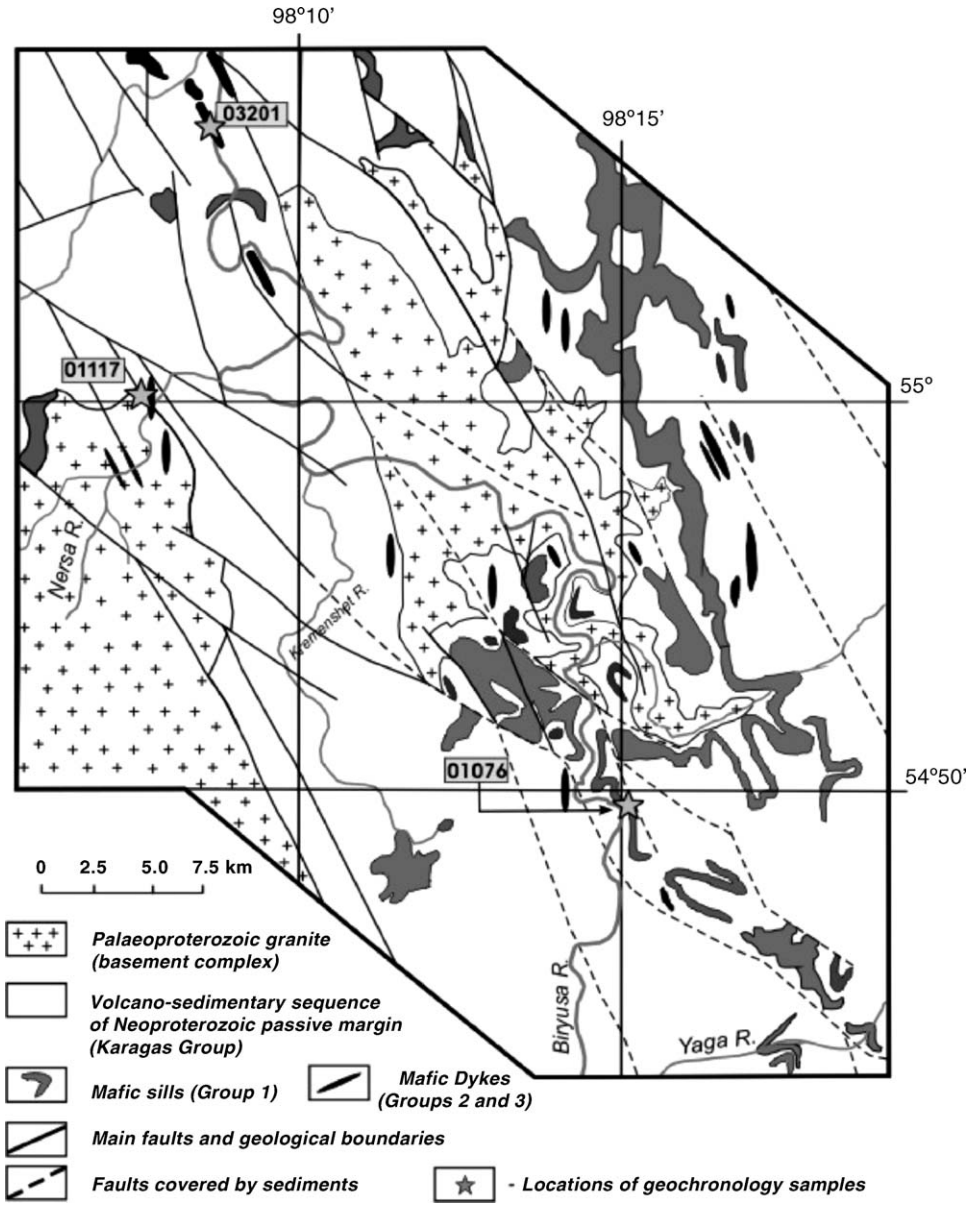


Fig. 2. Geological map of the Biryusa area, showing locations of geochronology samples.

precise age is debated (e.g. Khomentovsky, 1990, 2002; Sovetov, 2002). Thicknesses of both the Karagas and Oselkovaya Groups increase to the southwest, broadly consistent with the existence of a Neoproterozoic passive margin along the southwestern Siberian boundary (Sklyarov et al., 2001; Pisarevsky and Natapov, 2003). The Oselkovaya Group has also been interpreted as a foreland basin formed during accretionary orogenesis (Sovetov, 2002).

Three main groups of dolerite and gabbro intrusions are widespread in the Biryusa massif (Fig. 2). All have undergone moderate alteration; plagioclase is partly sericitised, and pyroxene is partly replaced by amphibole, biotite, and chlorite. The lower and middle parts of the Karagas Group are intruded by dolerite sills up to 100 m thick (Group 1). Thicker sills have coarse-grained centres and fine-grained chilled margins. Ophitic and subophitic textures are common between plagioclase (An 40–60) and clinopyroxene. Olivine, mainly altered to serpentine, occurs in the centres of some thick sills. Accessory minerals include interstitial brown biotite, amphibole, chlorite, quartz, titanite, Fe–Ti oxides, and apatite. Some sills in the middle Karagas Group exhibit evidence of intrusion into wet, unconsolidated sediment (Domyshev, 1976). Mafic sills are not found in the upper part of the Karagas Group, nor in the overlying Oselkovaya Group, implying that deposition of these strata postdates Group 1 igneous activity. The occurrence of dolerite pebbles in basal breccia of the Techinsk Formation of the uppermost Karagas Group (Domyshev, 1976) also supports this suggestion.

Mafic dykes are intruded into both basement rocks and the entire Karagas Group, and trend mainly subparallel to regional fault systems. North-trending dolerite dykes (Group 2) are typically 10–20 m wide and fine-grained. They are ophitic in texture and contain plagioclase (An 50–56), clinopyroxene, and minor late-crystallized brown hornblende. Interstitial accessory minerals include biotite, chlorite, quartz, Fe–Ti oxides, apatite, and zircon. Northwest-trending dolerite dykes (Group 3) are up to 50 m wide, and consist of ophitic plagioclase (An 50–56) and clinopyroxene, with minor orthopyroxene, late hornblende, and biotite, and interstitial quartz, chlorite, albite, apatite, titanite, zircon, and Fe–Ti oxides. The centres of most Group 3 dykes are medium- to coarse-grained, and some dyke centres contain abundant orthoclase.

No previous geochronology has been reported for mafic intrusions in the Biryusa massif, and relative ages from field relations are uncertain owing to an absence of exposed cross-cutting relationships. In the nearby Sharyzhalgai massif (Fig. 1), Sklyarov et al. (2003) identified northwest-trending mafic dykes, one of which yielded a $^{40}Ar/^{39}Ar$ plagioclase age of $758 \pm 4$ Ma and a Sm–Nd mineral isochron age of $743 \pm 47$ Ma.

## 3. Ar–Ar and U–Pb geochronology

Three fresh samples, one from each group, were selected for geochronology. Sample locations are shown in Fig. 2. Sample 01076, of medium-grained dolerite, was collected from the central part of a 60 m thick Group 1 sill intruded into the lower Karagas Group. The grain size of plagioclase used for $^{40}Ar$–$^{39}Ar$ analyses varied from 200 to 400 μm. Sample 01117 (Group 2) is from a fine- to medium-grained dolerite dyke intruded into middle Karagas sedimentary rocks, and yielded plagioclase grains 300–400 μm in size. About 400 zircons for U–Pb geochronology were separated from 1 kg of sample 03201 (Group 3), which is a very coarse-grained, highly fractionated phase from the centre of a 40 m-thick dolerite dyke also intruded into the middle Karagas Group. Plagioclase and zircon crystals were concentrated from crushed samples by standard density and magnetic techniques, followed by hand-picking.

### 3.1. Plagioclase $^{40}Ar$–$^{39}Ar$ step-heating results

Only transparent grains of plagioclase (mineral purity 99%) were selected for $^{40}Ar$–$^{39}Ar$ analyses to avoid the effects of secondary alteration. Measurements were conducted at the United Institute of Geology, Geophysics, and Mineralogy, Novosibirsk. Each sample was heated progressively and each heating step was maintained for 20 min. At each extraction temperature, the gas released was purified and analysed using gas source mass spectrometers, operated in the static mode RGA-10. International standards MSA-11, calibrated on Hd-Bio, and LP-6-Bio, were used. Ages were calculated according to Fleash et al. (1977), and uncertainties were calculated according to Dalrymple and Lanphere (1971). Table 1 lists $^{40}Ar/^{39}Ar$ thermochronology results for plagioclase from samples 01076 and 01117.

Step-heating of Group 1 sill sample 01076 provided a relatively well defined plateau age of $741.2 \pm 1.9$ Ma ($1\sigma$), based on 72.9% of the cumulative $^{39}Ar$ released (Fig. 3A). Group 2 dyke sample 01117 also yielded a well defined plateau, and an age of $611.7 \pm 3.1$ Ma ($1\sigma$), based on 80.3% of released $^{39}Ar$ (Fig. 3B). Both samples are from relatively thin intrusions that were emplaced at shallow depths, and probably cooled very quickly, hence we consider the $^{40}Ar/^{39}Ar$ ages ($\pm 2\sigma$) of $741 \pm 4$ Ma and $612 \pm 6$ Ma, for Group 1 sills and Group 2 dykes, respectively, to be good estimates of their times of emplacement

Table 1
Results of $^{40}Ar$–$^{39}Ar$ step-heating analysis of dolerite samples 01076 (Group 1) and 01117 (Group 2)

| Step | $T$ (°C) | Age | | $^{40}Ar/^{39}Ar$ | | $^{38}Ar/^{39}Ar$ | | $^{37}Ar/^{39}Ar$ | | $^{36}Ar/^{39}Ar$ | | Cumulative $^{39}Ar$ (%) |
|---|---|---|---|---|---|---|---|---|---|---|---|---|
| | | (Ma) | (±1σ) | | (±1σ) | | (±1σ) | | (±1σ) | | (±1σ) | |
| Sample 01076 | | | | | | | | | | | | |
| 1 | 550 | 678.5 | 3.5 | 89.2 | 0.4 | 0.045 | 0.0012 | 3.23 | 0.047 | 0.037 | 0.0013 | 7.37 |
| 2 | 600 | 687.4 | 3.6 | 90.6 | 0.5 | 0.081 | 0.0032 | 2.70 | 0.041 | 0.184 | 0.0013 | 11.0 |
| 3 | 650 | 742.8 | 4.8 | 99.5 | 0.7 | 0.048 | 0.0026 | 2.03 | 0.020 | 0.082 | 0.0022 | 15.9 |
| 4 | 700 | 738.9 | 3.4 | 98.9 | 0.4 | 0.049 | 0.0006 | 1.10 | 0.014 | 0.049 | 0.0006 | 32.6 |
| 5 | 820 | 740.3 | 3.1 | 99.1 | 0.3 | 0.038 | 0.0005 | 0.872 | 0.0066 | 0.026 | 0.0008 | 58.0 |
| 6 | 860 | 746.5 | 5.0 | 100.1 | 0.7 | 0.041 | 0.0014 | 0.837 | 0.0130 | 0.024 | 0.0016 | 79.4 |
| 7 | 940 | 707.3 | 3.2 | 93.7 | 0.4 | 0.054 | 0.0006 | 1.20 | 0.011 | 0.039 | 0.0010 | 93.4 |
| 8 | 1020 | 599.6 | 9.7 | 77.0 | 1.4 | 0.097 | 0.0016 | 3.01 | 0.019 | 0.068 | 0.0047 | 100.0 |
| Sample 01117 | | | | | | | | | | | | |
| 1 | 550 | 807.7 | 7.9 | 135.1 | 1.4 | 0.079 | 0.0034 | 5.00 | 0.226 | 0.092 | 0.0011 | 6.8 |
| 2 | 600 | 611.3 | 6.8 | 88.6 | 1.0 | 0.054 | 0.0029 | 3.38 | 0.051 | 0.039 | 0.0016 | 26.5 |
| 3 | 650 | 603.9 | 8.6 | 85.0 | 1.4 | 0.025 | 0.0018 | 1.83 | 0.111 | 0.030 | 0.0011 | 44.4 |
| 4 | 700 | 619.7 | 6.1 | 93.0 | 0.6 | 0.022 | 0.0054 | 2.33 | 0.295 | 0.049 | 0.0024 | 47.4 |
| 5 | 750 | 617.0 | 11.1 | 89.4 | 1.8 | 0.018 | 0.0031 | 1.61 | 0.088 | 0.039 | 0.0014 | 57.0 |
| 6 | 800 | 595.3 | 7.3 | 81.7 | 1.1 | 0.014 | 0.0017 | 1.46 | 0.049 | 0.023 | 0.0009 | 65.7 |
| 7 | 860 | 622.1 | 7.9 | 85.9 | 1.2 | 0.024 | 0.0009 | 1.84 | 0.043 | 0.024 | 0.0006 | 80.3 |
| 8 | 910 | 842.6 | 11.7 | 126.0 | 2.1 | 0.052 | 0.0033 | 3.55 | 0.083 | 0.041 | 0.0010 | 91.8 |
| 9 | 960 | 1263.6 | 17.8 | 210.5 | 3.9 | 0.093 | 0.0080 | 6.38 | 0.144 | 0.056 | 0.0012 | 97.1 |
| 10 | 1020 | 1515.3 | 15.4 | 287.4 | 4.1 | 0.153 | 0.0074 | 10.1 | 0.2 | 0.121 | 0.0026 | 100.0 |

The value of the irradiation parameter, $J$, is 0.00512 ± 0.00002 (1σ) for sample 01076 and 0.00531 ± 0.00002 (1σ) for sample 01117.

and crystallisation. Both $^{40}Ar/^{39}Ar$ ages are older than the U–Pb age of 511 Ma for Group 3 dykes in the same area (see below), implying that at least the younger of the Ar–Ar ages is primary.

### 3.2. SHRIMP U–Pb zircon results

At least three distinct types of zircon are present in Group 3 dyke sample 03201. About 30% (Type A) are small, equant to short (aspect ratios up to 3:1), clear, and colourless. Although variably rounded, they are generally subhedral, with well developed prism faces. A few show columnar growth habits, with multiple terminations. They do not exhibit concentric growth zoning, although several appear to contain distinct euhedral cores, and relatively thick (up to 30 μm) featureless rims, separated, in some zircons, from the core by a thin crack or cavity. The majority of the zircons (Type B, about 50%) are light to dark brown with prominent euhedral growth zoning, and either large (up to 350 mm long) and elongate (aspect ratios up to 8:1) or more equant and subhedral to irregular. The remaining zircons (Type C, about 20%) are equant and irregular in shape, rounded, mainly clear, and light yellow, and many are transected by large fractures.

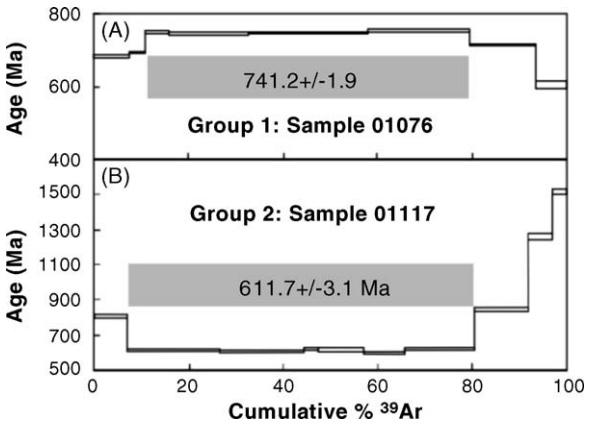


Fig. 3. $^{40}Ar/^{39}Ar$ apparent age spectra for (A) Group 1 sill sample 01076 and (B) Group 2 dyke sample 01117.

All zircons were cast, together with a zircon reference standard, in an epoxy disc, which was then polished to expose the interiors of the crystals. After cleaning, the sample mount was vacuum-coated with ~500 nm Au and loaded into the SHRIMP sample lock to pump down to high vacuum for 24 h prior to analysis. Twenty analyses of 19 zircons were collected during two sessions (Table 2), using operating and data reduction procedures similar to those described by Claoué-Long et al. (1995). Absolute U and Th concentrations and $^{238}U/^{206}Pb$ ratios in zircons were determined relative to the CZ3 zircon standard ($^{206}Pb/^{238}U = 0.9142$ [564 Ma],

Table 2
Ion microprobe U–Pb analytical data for zircons from dolerite sample 03201

| Grain | $^{238}$U (ppm) | $^{232}$Th (ppm) | Th/U | $f$206 (%) | $^{238}$U/$^{206}$Pb | | $^{207}$Pb/$^{206}$Pb | | $^{238}$U/$^{206}$Pb age | | $^{207}$Pb/$^{206}$Pb age | |
|---|---|---|---|---|---|---|---|---|---|---|---|---|
| | | | | | (Ma) | (±1$\sigma$) | | (±1$\sigma$) | | (±1$\sigma$) | | (±1$\sigma$) |
| 1.1 | 3186 | 7303 | 2.29 | 2.280 | 11.139 | 0.229 | 0.07959 | 0.00114 | 554 | 11 | 1187 | 28 |
| 3.1 | 520 | 129 | 0.25 | 1.599 | 12.933 | 0.147 | 0.05339 | 0.00151 | 480.1 | 5.3 | 345 | 63 |
| 4.1 | 449 | 183 | 0.41 | 0.100 | 12.092 | 0.123 | 0.05819 | 0.00085 | 512.2 | 5.0 | 537 | 32 |
| 5.1 | 45 | 25 | 0.56 | 2.737 | 10.017 | 0.267 | 0.05089 | 0.01426 | 613 | 16 | 236 | 543 |
| 6.1 | 398 | 163 | 0.41 | 0.183 | 11.926 | 0.150 | 0.05707 | 0.00121 | 519.1 | 6.3 | 494 | 46 |
| 7.1 | 743 | 50 | 0.07 | 0.018 | 13.107 | 0.155 | 0.05620 | 0.00065 | 474.0 | 5.4 | 461 | 26 |
| 7.2 | 518 | 165 | 0.32 | 0.002 | 12.257 | 0.119 | 0.05722 | 0.00095 | 505.6 | 4.7 | 500 | 36 |
| 8.1 | 504 | 239 | 0.47 | 0.099 | 12.257 | 0.119 | 0.05586 | 0.00063 | 505.6 | 4.7 | 447 | 25 |
| 9.1 | 3360 | 9750 | 2.90 | 0.525 | 10.058 | 0.178 | 0.06813 | 0.00079 | 611 | 10 | 873 | 24 |
| 10.1 | 3222 | 4355 | 1.35 | 0.589 | 7.223 | 0.124 | 0.08214 | 0.00038 | 836 | 13 | 1248.8 | 9.0 |
| 11.1 | 1115 | 1189 | 1.07 | 0.113 | 4.095 | 0.021 | 0.09652 | 0.00041 | 1408.4 | 6.4 | 1557.8 | 7.9 |
| 12.1 | 326 | 170 | 0.52 | 0.283 | 11.828 | 0.148 | 0.06056 | 0.00284 | 523.2 | 6.3 | 624 | 98 |
| 13.1 | 747 | 378 | 0.51 | 0.238 | 12.329 | 0.141 | 0.05677 | 0.00064 | 502.7 | 5.5 | 483 | 25 |
| 14.1 | 212 | 84 | 0.40 | 0.015 | 3.123 | 0.027 | 0.10843 | 0.00101 | 1791 | 13 | 1773 | 17 |
| 15.1 | 514 | 87 | 0.17 | 0.593 | 13.535 | 0.207 | 0.05594 | 0.00329 | 459.5 | 6.8 | 450 | 126 |
| 16.1 | 521 | 201 | 0.39 | 0.003 | 3.169 | 0.025 | 0.11260 | 0.00087 | 1768 | 12 | 1842 | 14 |
| 17.1 | 928 | 360 | 0.39 | 0.185 | 4.182 | 0.034 | 0.11252 | 0.00083 | 1382 | 10 | 1841 | 13 |
| 18.1 | 315 | 130 | 0.41 | 0.173 | 12.409 | 1.184 | 0.05678 | 0.00513 | 500 | 46 | 483 | 188 |
| 19.1 | 246 | 186 | 0.76 | 0.023 | 2.879 | 0.102 | 0.11472 | 0.00258 | 1922 | 59 | 1876 | 40 |
| 20.1 | 502 | 186 | 0.37 | 0.029 | 11.837 | 0.391 | 0.05695 | 0.00298 | 523 | 17 | 489 | 112 |

Ratios and ages are corrected for common Pb using $^{204}$Pb; $f$206 is the proportion of common $^{206}$Pb in measured $^{206}$Pb. Uncertainties in $^{238}$U/$^{206}$Pb ratios and ages do not include calibration uncertainties (1$\sigma$) of 0.82% for #1–17, and 0.58% for #18–20, which should be added in quadrature when reporting the 'absolute' mean $^{238}$U/$^{206}$Pb age for a group of analyses.

550 ppm $^{238}$U), analyses of which were interspersed with those of unknown zircons. Common Pb correction using non-radiogenic $^{204}$Pb employed an average crustal common Pb composition appropriate to the age of the mineral.

The analyses fall into two groups: a mainly concordant group at about 500 Ma which was obtained from Type A zircons, and a variably discordant group aligned roughly along a discordia between about 1900 Ma and 500 Ma, obtained from Type B zircons. No Type C zircons were analysed. One analysis (#5.1), which has the lowest U content (45 ppm), highest common Pb (2.7% common $^{206}$Pb), and is strongly reversely discordant, is excluded from further consideration.

The eleven Type A zircons in the concordant group (square symbols, Fig. 4) have moderate $^{238}$U contents between 315 and 750 ppm, $^{232}$Th contents between 50 and 380 ppm, and mostly consistent Th/U ratios, averaging about 0.4 (Table 2). Common $^{206}$Pb is low, up to 1.6%, with a median of 0.17%. Eight of 11 zircons have $^{238}$U/$^{206}$Pb ratios, corrected for common Pb, that agree to within analytical precision and yield a mean age of 510.8 ± 2.7 Ma (1$\sigma$, MSWD = 1.03). A regression through data uncorrected for common Pb, anchored at initial Pb ($^{207}$Pb/$^{206}$Pb = 0.89 at 511 Ma), yields a Concordia intercept age and uncertainty identical to the 204-corrected result. In each case, three excluded analyses are significantly younger and interpreted to have lost small amounts of radiogenic Pb. An age of 511 ± 5 Ma (95% confidence interval, and including

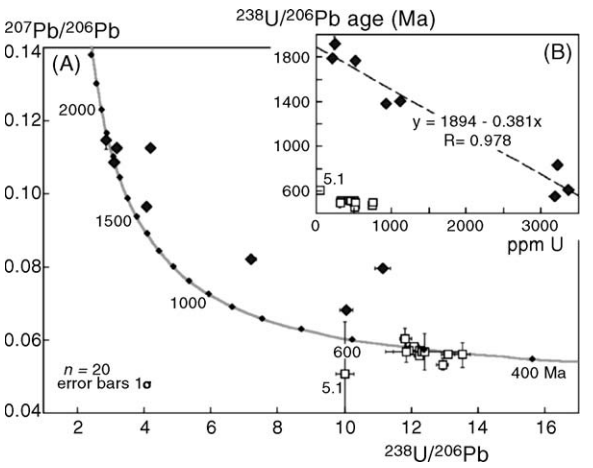


Fig. 4. (A) U–Pb evolution (Concordia) diagram showing analytical data for Group 3 dyke sample 03201. All data are corrected for common Pb using $^{204}$Pb. Analyses of xenocrystic zircons are shown by shaded diamond symbols; those of primary zircons (interpreted to have formed in the dyke) are shown by open squares. (B) Variation of U/Pb age with $^{238}$U concentration, showing best fit line to xenocrystic zircon analyses. R, Pearson's correlation coefficient.

calibration uncertainty) is the best estimate of the time of crystallisation of Type A zircons.

The remaining eight analyses of Type B zircons (filled diamonds, Fig. 4) range from concordant to very strongly discordant. U content ranges from 200 to 3360 ppm, Th varies from 84 to 9750 ppm, and Th/U ratios range from 0.4 to 2.9 (Table 2). U/Pb ages correlate closely with $^{238}U$ content (Fig. 4B), indicating that discordance is mainly due to loss of radiogenic Pb from radiation-damaged crystals. The two concordant analyses yield $^{207}Pb/^{206}Pb$ ages of 1876 and 1773 Ma. Zircons in this group are interpreted to be xenocrysts inherited from basement rocks of Paleoproterozoic age. The pattern of discordance is broadly consistent with Pb loss being mainly the result of incorporation of the xenocrysts into the mafic magma during dyke emplacement at 511 Ma.

## 4. Geochemical characteristics of mafic intrusions

More than 80 fresh dolerite samples from different localities were collected for geochemical analysis. Major, trace, and rare-earth element (REE) analyses for several representative intrusions in each of Groups 1–3 are presented in Tables 3 and 4. Owing to the possibility of element mobilization during late alteration, we concentrated mainly on elements that are relatively immobile during metamorphism (Zr, Nb, Y, Ti, and REE). Major elements were determined at the United Institute of Geology and Geophysics, Novosibirsk, by X-ray fluorescence spectrometry (XRF). Abundances of Cr, Ni, Co, Sc, and V were determined by XRF at the Institute of the Earth's Crust, Irkutsk. Other trace elements and rare earth elements (REE) were determined by inductively coupled plasma mass spectrometry (ICP-MS) using a VG Plasmaquad PQ-2 Plus (VG Elemental) in the Limnological Institute, Irkutsk. Instrument configuration, operating conditions, and the acid dissolution technique used to prepare the samples for ICP-MS analysis were described by Garbe-Schonberg (1993). Calibrations were set using internal standards and international rock standards (BHVO-1, BIR-1, W-2, RGM-1). Precision and accuracy are 0.5–1.0% for major elements and up to 5% for trace elements and REE.

### 4.1. Geochemical classification

Chemically, most analysed samples are sub-alkalic basalt to andesite-basalt (Fig. 5), although their major element concentrations vary significantly (Figs. 5–7). The three groups of intrusions, defined above on the basis of orientation, petrography, and isotopic age, are also readily distinguished by major element concentrations, $Fe_2O_3t$ (=$Fe_2O_3 + 1.1^*FeO$) content, and Nb/La and Zr/Th ratios (Fig. 6A and B):

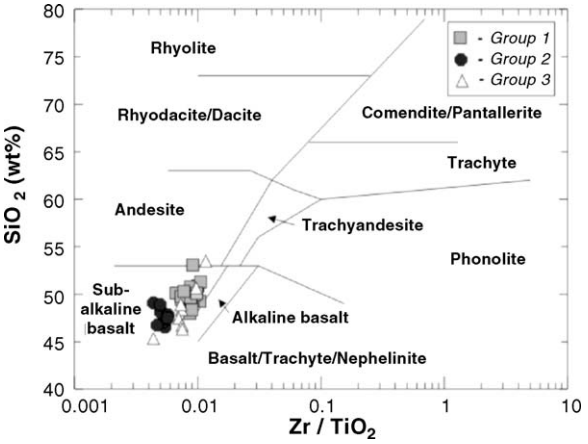


Fig. 5. Classification of dolerites using a $SiO_2$–$Zr/TiO_2$ diagram (Winchester and Floyd, 1977).

- Group 1 sills (grey squares) fall within the field of high-Mg tholeiite (HMT) in Fig. 7. They have rather low $Fe_2O_3t$ (10.26–13.69) and moderate Nb/La (0.46–0.59) and Zr/Th (24–32).
- North-trending Group 2 dykes (black circles) plot near the HMT-HFT (high-Fe tholeiite) boundary in Fig. 7.

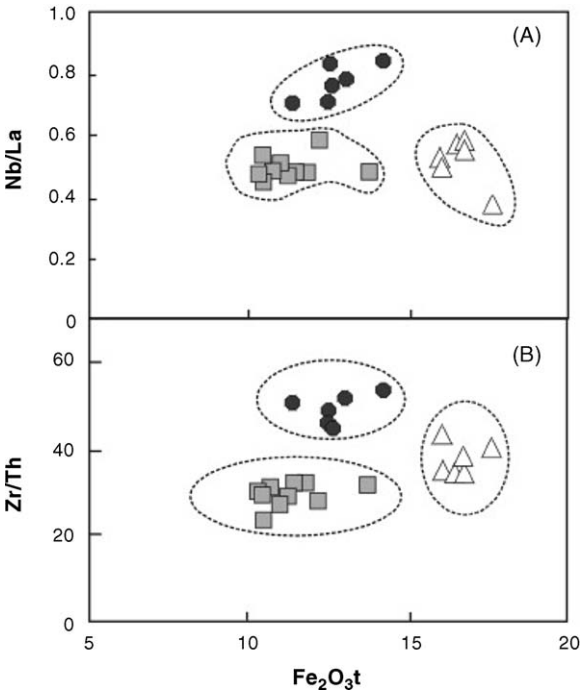


Fig. 6. Classification of dolerites using (A) Nb/La–$Fe_2O_3t$ and (B) Zr/Th–$Fe_2O_3t$ diagrams. Symbols as in Fig. 5.

Table 3
Geochemical compositions of Group 1 sills

| | Samples | | | | | | | | | |
|---|---|---|---|---|---|---|---|---|---|---|
| | 01061 | 01064 | 01069 | 01071 | 01073 | 01076 | 01090 | 02101 | 02125 | 02126 |
| $SiO_2$ | 49.56 | 49.24 | 49.92 | 50.79 | 50.10 | 49.74 | 49.64 | 50.28 | 51.30 | 50.08 |
| $TiO_2$ | 0.93 | 0.93 | 1.02 | 1.20 | 1.16 | 1.03 | 1.08 | 0.90 | 1.51 | 1.12 |
| $Al_2O_3$ | 13.42 | 15.15 | 14.80 | 14.80 | 13.22 | 14.40 | 12.86 | 15.00 | 13.16 | 14.40 |
| $Fe_2O_3t$ | 10.35 | 10.26 | 10.63 | 11.35 | 11.17 | 10.91 | 12.14 | 10.40 | 13.69 | 11.75 |
| MnO | 0.18 | 0.14 | 0.15 | 0.13 | 0.14 | 0.15 | 0.19 | 0.18 | 0.19 | 0.18 |
| MgO | 9.58 | 7.81 | 7.00 | 6.70 | 10.05 | 9.47 | 11.07 | 7.37 | 6.41 | 7.35 |
| CaO | 9.39 | 9.14 | 8.53 | 7.03 | 4.60 | 8.94 | 9.12 | 9.79 | 7.79 | 8.53 |
| $Na_2O$ | 1.11 | 2.01 | 2.68 | 2.18 | 0.62 | 1.93 | 0.40 | 2.31 | 2.54 | 2.53 |
| $K_2O$ | 1.77 | 2.04 | 1.88 | 1.87 | 3.79 | 1.32 | 1.48 | 1.95 | 1.66 | 2.01 |
| $P_2O_5$ | 0.09 | 0.11 | 0.10 | 0.12 | 0.11 | 0.10 | 0.12 | 0.07 | 0.16 | 0.12 |
| LOI | 2.53 | 2.91 | 3.10 | 2.96 | 3.68 | 2.49 | 1.78 | 2.59 | 1.77 | 1.59 |
| Total | 98.91 | 99.74 | 99.81 | 99.13 | 98.64 | 100.48 | 99.88 | 100.84 | 100.18 | 99.66 |
| Mg# | 64.7 | 60.1 | 56.6 | 53.9 | 64.1 | 63.2 | 64.4 | 58.4 | 48.1 | 55.3 |
| Rb | 58.8 | 73.4 | 74.1 | 47.8 | 90.2 | 24.7 | 44.0 | 82.3 | 36.6 | 63.7 |
| Sr | 190 | 246 | 176 | 213 | 206 | 179 | 189 | 253 | 232 | 220 |
| Y | 18.5 | 20.1 | 19.7 | 22.9 | 20.0 | 17.8 | 20.7 | 16.0 | 30.9 | 23.2 |
| Zr | 85.4 | 97.1 | 96.3 | 105 | 77.5 | 75.4 | 95.1 | 69.6 | 159 | 110 |
| Nb | 7.49 | 7.20 | 7.12 | 8.12 | 7.58 | 6.72 | 9.12 | 6.78 | 13.0 | 9.87 |
| Ba | 313 | 531 | 491 | 457 | 442 | 303 | 253 | 423 | 411 | 767 |
| Co | 54 | 34 | 55 | 39 | 49 | 51 | 56 | 39 | 46 | 60 |
| Ni | 220 | 130 | 140 | 86 | 170 | 220 | 230 | 130 | 64 | 100 |
| Sc | 35 | 25 | 55 | 30 | 69 | 15 | 54 | 35 | 38 | 40 |
| V | 320 | 210 | 260 | 170 | 320 | 200 | 240 | 200 | 250 | 250 |
| Cr | 240 | 180 | 290 | 140 | 270 | 250 | 300 | 310 | 24 | 190 |
| La | 13.9 | 15.1 | 14.5 | 16.8 | 15.7 | 13.1 | 15.4 | 14.7 | 26.6 | 20.3 |
| Ce | 29.9 | 31.2 | 30.3 | 34.7 | 33.0 | 27.7 | 33.2 | 29.6 | 53.1 | 39.2 |
| Pr | 3.66 | 4.16 | 4.00 | 4.68 | 4.09 | 3.80 | 4.12 | 3.42 | 6.18 | 4.57 |
| Nd | 14.7 | 16.6 | 16.4 | 18.5 | 16.3 | 15.5 | 16.4 | 15.8 | 24.5 | 18.3 |
| Sm | 3.50 | 3.57 | 3.46 | 4.14 | 3.96 | 3.24 | 3.91 | 3.98 | 4.92 | 3.82 |
| Eu | 0.96 | 1.08 | 0.96 | 1.18 | 1.05 | 1.02 | 1.03 | 1.02 | 1.53 | 1.22 |
| Gd | 3.35 | 3.41 | 3.49 | 3.89 | 3.49 | 3.51 | 3.63 | 3.40 | 5.41 | 3.83 |
| Tb | 0.53 | 0.55 | 0.55 | 0.62 | 0.59 | 0.54 | 0.58 | 0.60 | 0.98 | 0.70 |
| Dy | 3.22 | 3.22 | 3.23 | 3.73 | 3.48 | 3.27 | 3.60 | 3.00 | 4.96 | 3.66 |
| Ho | 0.68 | 0.71 | 0.70 | 0.78 | 0.68 | 0.72 | 0.74 | 0.62 | 0.98 | 0.72 |
| Er | 1.95 | 1.78 | 1.83 | 2.11 | 2.04 | 1.83 | 2.10 | 1.88 | 3.06 | 2.24 |
| Tm | 0.28 | 0.29 | 0.30 | 0.36 | 0.31 | 0.32 | 0.32 | 0.27 | 0.49 | 0.35 |
| Yb | 1.78 | 1.75 | 1.73 | 1.95 | 1.77 | 1.85 | 1.86 | 1.84 | 2.78 | 2.06 |
| Lu | 0.24 | 0.26 | 0.25 | 0.29 | 0.25 | 0.28 | 0.28 | 0.26 | 0.42 | 0.30 |
| Hf | 2.43 | 2.42 | 2.45 | 2.44 | 2.26 | 2.20 | 2.67 | 2.14 | 4.13 | 2.66 |
| Ta | 0.89 | 0.62 | 0.56 | 0.69 | 0.95 | 0.65 | 1.05 | 0.45 | 0.77 | 0.56 |
| Pb | 0.40 | 0.13 | 0.11 | 0.16 | 0.31 | 0.17 | 0.38 | 1.94 | 4.01 | 3.43 |
| Th | 2.92 | 3.22 | 3.10 | 3.31 | 2.63 | 2.82 | 3.38 | 2.94 | 5.01 | 3.41 |
| U | 0.47 | 0.50 | 0.50 | 0.52 | 0.42 | 0.47 | 0.58 | 0.49 | 0.82 | 0.58 |
| Nb/La | 0.54 | 0.48 | 0.49 | 0.48 | 0.48 | 0.51 | 0.59 | 0.46 | 0.49 | 0.49 |
| Zr/Th | 29.3 | 30.2 | 31.1 | 31.7 | 29.4 | 26.7 | 28.1 | 23.7 | 31.8 | 32.2 |
| Th/Ce | 0.10 | 0.10 | 0.10 | 0.10 | 0.08 | 0.10 | 0.10 | 0.10 | 0.09 | 0.09 |
| Th/Ta | 3.28 | 5.19 | 5.52 | 4.78 | 2.78 | 4.32 | 3.22 | 6.57 | 6.47 | 6.04 |
| Nb/U | 15.8 | 14.3 | 14.1 | 15.7 | 18.1 | 14.2 | 15.9 | 13.9 | 15.8 | 17.0 |
| $(La/Yb)_n$ | 5.19 | 5.79 | 5.60 | 5.78 | 5.94 | 4.76 | 5.55 | 5.37 | 6.41 | 6.61 |
| $(Gd/Yb)_n$ | 1.50 | 1.55 | 1.61 | 1.60 | 1.57 | 1.52 | 1.55 | 1.48 | 1.55 | 1.48 |
| $Eu/Eu^*$ | 0.85 | 0.94 | 0.84 | 0.89 | 0.85 | 0.93 | 0.83 | 0.83 | 0.91 | 0.97 |

Table 4
Geochemical compositions of Group 2 and 3 dykes

| | Samples | | | | | | | | | |
|---|---|---|---|---|---|---|---|---|---|---|
| | Group 2 | | | | | Group 3 | | | | |
| | 01088 | 01089 | 01117 | 01119 | 0294 | 02121 | 02122 | 02128 | 03201 | 02133 |
| $SiO_2$ | 47.05 | 46.74 | 49.09 | 47.96 | 48.09 | 48.90 | 47.46 | 46.04 | 53.78 | 46.32 |
| $TiO_2$ | 2.02 | 2.13 | 1.88 | 1.76 | 1.73 | 2.97 | 3.04 | 2.20 | 2.53 | 2.82 |
| $Al_2O_3$ | 13.46 | 13.28 | 14.8 | 14.74 | 14.45 | 11.55 | 12.92 | 13.90 | 13.08 | 12.25 |
| $Fe_2O_3t$ | 13.00 | 14.19 | 12.61 | 12.51 | 11.34 | 16.49 | 16.72 | 15.30 | 15.73 | 16.72 |
| MnO | 0.20 | 0.20 | 0.20 | 0.20 | 0.15 | 0.27 | 0.27 | 0.23 | 0.21 | 0.26 |
| MgO | 8.94 | 8.49 | 6.39 | 7.86 | 7.86 | 5.84 | 5.66 | 7.19 | 3.63 | 6.14 |
| CaO | 9.47 | 8.65 | 9.85 | 9.90 | 10.15 | 7.72 | 7.68 | 7.84 | 3.39 | 7.51 |
| $Na_2O$ | 1.58 | 2.20 | 2.35 | 1.53 | 2.08 | 1.77 | 2.58 | 2.31 | 3.78 | 3.25 |
| $K_2O$ | 0.79 | 1.23 | 0.93 | 1.21 | 0.86 | 1.81 | 2.10 | 2.13 | 1.72 | 2.06 |
| $P_2O_5$ | 0.25 | 0.23 | 0.18 | 0.21 | 0.17 | 0.67 | 0.72 | 0.21 | 0.55 | 0.36 |
| LOI | 1.90 | 2.44 | 1.95 | 1.34 | 2.96 | 1.80 | 1.71 | 1.84 | 2.05 | 2.03 |
| Total | 98.68 | 99.78 | 100.20 | 99.22 | 99.84 | 99.79 | 100.87 | 99.18 | 100.45 | 99.73 |
| Mg# | 57.7 | 54.2 | 50.1 | 55.5 | 57.9 | 41.2 | 40.1 | 48.2 | 31.4 | 42.1 |
| Rb | 15.7 | 27.0 | 29.8 | 34.4 | 23.9 | 120 | 128 | 50.8 | 31.2 | 79.7 |
| Sr | 275 | 272 | 278 | 327 | 334 | 199 | 211 | 320 | 161 | 238 |
| Y | 26.1 | 25.7 | 21.9 | 23.4 | 20.1 | 55.3 | 56.2 | 24.3 | 52.1 | 50.7 |
| Zr | 107 | 99.6 | 82.2 | 92.6 | 86.4 | 217 | 214 | 102 | 295 | 212 |
| Nb | 15.2 | 15.2 | 12.2 | 13.9 | 12.9 | 19.6 | 19.0 | 7.64 | 25.4 | 15.2 |
| Ba | 310 | 530 | 392 | 340 | 366 | 433 | 422 | 380 | 867 | 740 |
| Co | 39 | 44 | 32 | 40 | 40 | 41 | 50 | 53 | 38 | 40 |
| Ni | 58 | 68 | 46 | 46 | 79 | 43 | 56 | 55 | 3 | 64 |
| Sc | 20 | 28 | 31 | 46 | 40 | 55 | 60 | 43 | 32 | 50 |
| V | 250 | 250 | 220 | 230 | 180 | 290 | 300 | 450 | 85 | 310 |
| Cr | 70 | 57 | 73 | 26 | 280 | 31 | 40 | 52 | 6 | 83 |
| La | 19.4 | 18.0 | 16.0 | 16.7 | 18.3 | 34.4 | 32.7 | 18.4 | 45.4 | 27.9 |
| Ce | 42.7 | 40.1 | 34.5 | 37.2 | 38.1 | 70.4 | 68.0 | 39.4 | 91.6 | 57.9 |
| Pr | 5.48 | 5.24 | 4.79 | 4.84 | 4.57 | 8.74 | 8.46 | 5.34 | 11.4 | 7.02 |
| Nd | 23.1 | 22.1 | 20.4 | 20.6 | 21.8 | 36.5 | 35.8 | 21.1 | 47.4 | 30.2 |
| Sm | 5.49 | 5.65 | 4.50 | 5.02 | 5.60 | 8.28 | 8.06 | 4.75 | 10.8 | 7.21 |
| Eu | 1.75 | 1.68 | 1.53 | 1.61 | 1.63 | 2.47 | 2.39 | 1.56 | 3.22 | 2.14 |
| Gd | 5.23 | 4.87 | 4.55 | 4.69 | 4.70 | 9.21 | 9.24 | 4.49 | 12.0 | 8.19 |
| Tb | 0.84 | 0.80 | 0.67 | 0.77 | 0.81 | 1.69 | 1.66 | 0.70 | 2.20 | 1.56 |
| Dy | 4.92 | 4.50 | 3.94 | 4.21 | 3.92 | 8.83 | 8.91 | 4.21 | 11.5 | 8.40 |
| Ho | 0.94 | 0.91 | 0.86 | 0.86 | 0.75 | 1.81 | 1.83 | 0.64 | 2.35 | 1.73 |
| Er | 2.79 | 2.52 | 2.17 | 2.35 | 2.25 | 5.54 | 5.70 | 2.08 | 7.20 | 5.35 |
| Tm | 0.40 | 0.38 | 0.35 | 0.35 | 0.31 | 0.85 | 0.86 | 0.27 | 1.10 | 0.82 |
| Yb | 2.22 | 2.16 | 2.07 | 2.06 | 2.04 | 4.84 | 4.71 | 1.87 | 6.20 | 4.96 |
| Lu | 0.34 | 0.30 | 0.31 | 0.30 | 0.30 | 0.73 | 0.74 | 0.30 | 0.95 | 0.74 |
| Hf | 3.11 | 2.74 | 2.40 | 2.78 | 2.59 | 5.24 | 5.25 | 2.42 | 6.81 | 5.44 |
| Ta | 1.72 | 1.69 | 1.09 | 1.65 | 0.82 | 1.32 | 1.31 | 0.75 | 1.58 | 1.06 |
| Pb | 0.37 | 0.76 | 0.23 | 0.47 | 3.37 | 5.98 | 6.31 | 5.37 | 8.37 | 9.41 |
| Th | 2.08 | 1.87 | 1.86 | 1.91 | 1.71 | 6.43 | 6.23 | 1.68 | 7.07 | 5.61 |
| U | 0.46 | 0.41 | 0.44 | 0.40 | 0.41 | 1.43 | 1.14 | 0.38 | 1.86 | 1.48 |
| Nb/La | 0.78 | 0.84 | 0.76 | 0.83 | 0.71 | 0.57 | 0.58 | 0.42 | 0.56 | 0.54 |
| Zr/Th | 51.3 | 53.3 | 44.2 | 48.6 | 50.5 | 33.8 | 34.3 | 60.8 | 41.7 | 37.7 |
| Th/Ce | 0.05 | 0.05 | 0.05 | 0.05 | 0.04 | 0.09 | 0.09 | 0.04 | 0.08 | 0.10 |
| Th/Ta | 1.21 | 1.11 | 1.70 | 1.16 | 2.09 | 4.88 | 4.74 | 2.23 | 4.47 | 5.32 |
| Nb/U | 33.0 | 36.9 | 27.6 | 34.7 | 31.7 | 13.7 | 16.7 | 20.2 | 13.6 | 10.3 |
| $(La/Yb)_n$ | – | 5.58 | 5.16 | 5.41 | 5.99 | 4.75 | 4.65 | 6.56 | 4.90 | 3.76 |
| $(Gd/Yb)_n$ | 1.88 | 1.80 | 1.75 | 1.81 | 1.84 | 1.51 | 1.56 | 1.91 | 1.54 | 1.32 |
| $Eu/Eu^*$ | 0.99 | 0.96 | 1.03 | 1.01 | 0.95 | 0.87 | 0.85 | 1.02 | 0.87 | 0.85 |

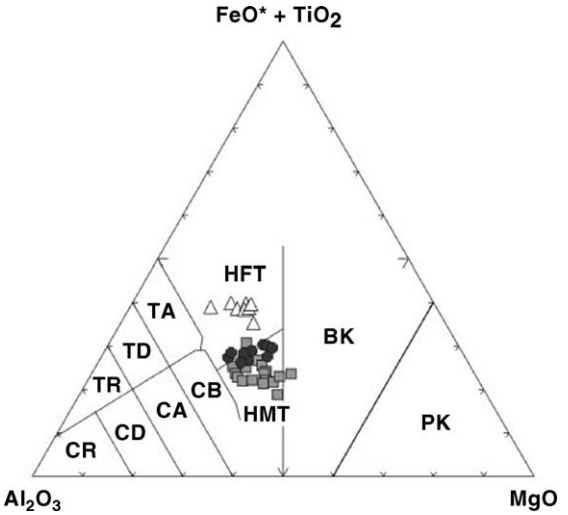


Fig. 7. Classification of dolerites using an $Al_2O_3$–$FeO^*$ + $TiO_2$–MgO diagram (Jensen, 1976) for classification of dolerites. TR, tholeiitic rhyolite; TD, tholeiitic dacite; TA, tholeiitic andesite; CR, calc-alkaline rhyolite; CD, calc-alkaline dacite; CA, calc-alkaline andesite; CB, calc-alkaline basalt; HFT, high-Fe tholeiite; HMT, high-Mg tholeiite; BK, basaltic komatiite; PK, peridotitic komatiite. Symbols as in Fig. 5.

They have moderate values of $Fe_2O_3t$ (11.34–14.19), high Nb/La (0.71–0.84), and high Zr/Th (44–53).

- Northwest-trending Group 3 dykes (triangles) fall in the HFT field in Fig. 7. They have the highest $Fe_2O_3t$ (15.30–16.72), intermediate Nb/La (0.37–0.58), and variable Zr/Th (34–42).

### 4.2. Major and trace element abundances

All three groups of intrusions show some variation in major oxide contents and incompatible element abundances with the differentiation index Mg# ($=100 \times Mg^{2+}/[Mg^{2+} + Fe^{2+} + Fe^{3+}]$), indicating changes in major and trace element patterns with increasing differentiation (Fig. 8). The highest Mg# values are characteristic of Group 1 (squares, Fig. 8); several with Mg# ≥64 may represent primary mantle-derived magmas. Group 1 samples have lower concentrations of incompatible elements, such as $TiO_2$, $P_2O_5$, and Nb, and high abundances of Ni. Several elements show significant variation within thick sills (e.g. Mg# and Ni (Table 3, samples 01061, 01064, and 01069 from one sill and 01071, 01073, and 01076 from another). These variations can be explained by flow differentiation during emplacement. Group 2 samples (circles, Fig. 8) have Mg# between 50 and 58, similar to those of partially evolved Group 1 samples, and have higher contents of $TiO_2$, $P_2O_5$, and Nb. However, these values are lower than those of Group 3 samples (triangles, Fig. 8). Th contents in Group 2 dykes are low compared to Groups 1 and 3. In contrast to Group 1, Group 3 samples are evolved, with Mg# <50. All Group 3 samples are enriched in $Fe_2O_3t$, $TiO_2$, and Th, but depleted in Ni; most are also enriched in $P_2O_5$, Nb, and Y (Fig. 8). Trends of Mg# versus $SiO_2$ (Fig. 8A) are different for all three groups, suggesting that the three suites of intrusions had separate magma sources and evolution paths.

Trace element abundances are shown in the Th–Zr/117–Nb/16 ternary diagram of Wood (1980) (Fig. 9). Results for Groups 1 and 3 samples fall within the field of Destructive Plate Margin Basalts and their differentiates. In contrast, Group 2 samples correspond to E-type MORB basalts and within-plate tholeiites. Trace element patterns (spidergrams, Fig. 10), normalized to primitive mantle, also exhibit distinct variations in incompatible element composition between the three groups. Group 1 is characterized by distinct negative U, Nb–Ta, P, and Ti anomalies (Fig. 10A). In contrast, Group 2 shows more weakly negative Nb and P anomalies, a distinct Th–U anomaly, and no Ti and Ta anomalies (Fig. 10B). All Group 3 samples show a distinct negative Nb–Ta anomaly, and all but one exhibit negative Sr anomalies and no Th, U, P, or Ti anomalies (Fig. 10C).

### 4.3. Rare earth elements

Chondrite-normalized REE abundances are plotted in Fig. 11. All analysed samples are enriched in REE. Weakly negative Eu anomalies are characteristic of Group 1 ($Eu/Eu^* = 0.83$–$0.97$, Fig. 11A) and Group 3 ($Eu/Eu^* = 0.85$–$0.87$, Fig. 11C). This anomaly is absent in Group 2 ($Eu/Eu^* = 0.95$–$1.03$, Fig. 11B). Groups 1 and 2 show slight REE fractionation and REE-normalized abundance patterns of similar slope, with $(La/Yb)_n = 4.76$–$6.61$ and 5.16–5.99, respectively (Fig. 11). Group 3 samples have the highest REE contents and relatively flat REE-normalized abundance patterns with $(La/Yb)_n$ values of 3.76–4.75. A gently sloping HREE field is characteristic of Groups 1 and 3. $(Gd/Yb)_n$ ratios are 1.48–1.61 for Group 1 and 1.32–1.56 for Group 3. Group 2, in contrast, shows more steeply sloping HREE abundances and higher values of $(Gd/Yb)_n$, between 1.75 and 1.88.

## 5. Discussion

### 5.1. Ages of mafic intrusions and sedimentary rocks in SW Siberia

The $741 \pm 4$ Ma $^{40}Ar$–$^{39}Ar$ plagioclase age obtained for Group 1 sills in the Biryusa massif is similar to results

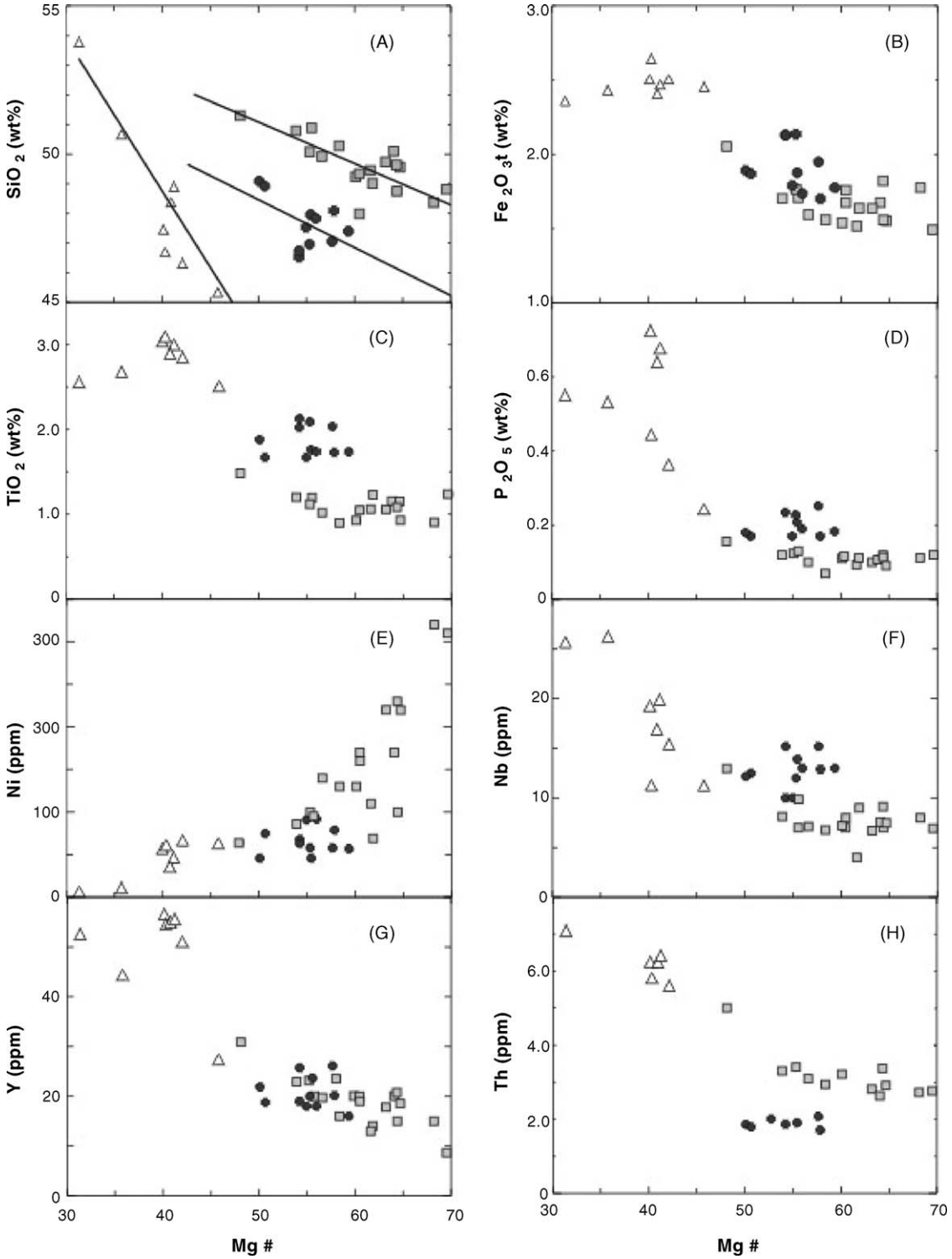


Fig. 8. Variation of $SiO_2$, $Fe_2O_3t$, $TiO_2$, $P_2O_5$, Ni, Nb, Y, and Th with magnesium number, Mg#. Symbols as in Fig. 5.

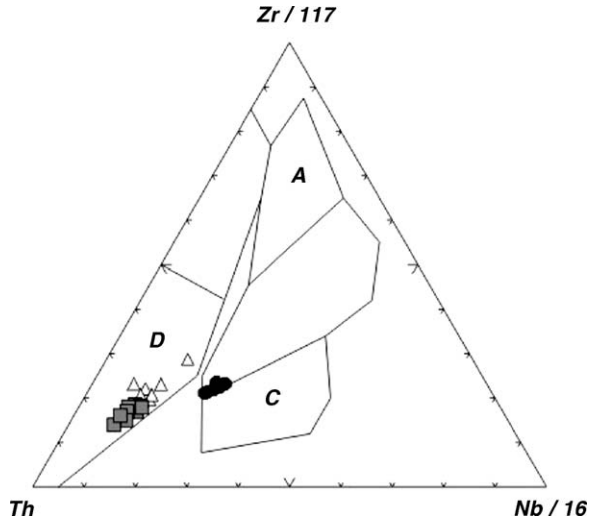


Fig. 9. Classification of dolerites using the Th–Zr/117–Nb/16 diagram (Wood, 1980). A, N-type MORB basalt; B, E-type MORB basalt and within-plate tholeiites; C, alkaline within-plate basalts and their differentiates; D, destructive plate-margin basalts and their differentiates. Symbols as in Fig. 5.

reported by Sklyarov et al. (2003) for dolerite dykes in the Sharyzhalgai massif further to the south. They obtained a $^{40}Ar$–$^{39}Ar$ plagioclase age of $758 \pm 4$ Ma and a Sm-Nd mineral isochron age of $743 \pm 47$ Ma for the youngest suite of dykes identified in that area. Although the Ar–Ar age for Group 1 sills is significantly younger than that of Sklyarov et al. (2003), those authors recommended that their result be used with caution, owing to the possibility of contamination by excess radiogenic Ar. The broad concordance of both Ar–Ar ages with the Sm–Nd result, however, suggests that mafic intrusions were emplaced into both the Sharyzhalgai and Biryusa massifs at about 740 Ma. The 741 Ma age for Group 1 sills also provides a younger limit for deposition of the lower and middle parts of the Karagas Group. Evidence for sill emplacement into wet sediment (Domyshev, 1976) implies that the middle Karagas Group was deposited at approximately 740 Ma.

Groups 2 and 3 dykes in the Biryusa massif are dated at $612 \pm 6$ and $511 \pm 5$ Ma, respectively. Northwest-trending Group 2 dykes intruded the upper Karagas Group, indicating that it was deposited between ~740 and 612 Ma. No intrusions are reported to have intruded the Oselkovaya Group. Although mafic intrusions younger than 740 Ma have not been identified in the Sharyzhalgai massif, and so may be restricted to the Biryusa block, there is scope for additional geochronological studies in both areas.

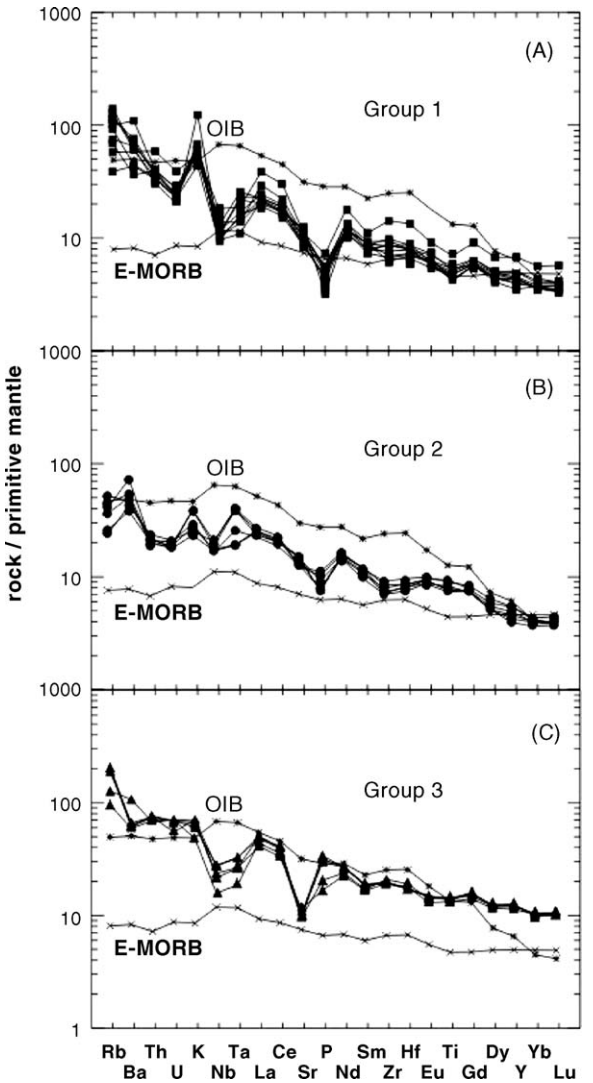


Fig. 10. Primitive mantle-normalised (Sun and McDonough, 1989) abundances of trace elements in dolerites.

### 5.2. Petrogenesis of mafic intrusions in the Biryusa massif

Group 1 dolerite sills exhibit pronounced negative Nb–Ta and Ti anomalies (Fig. 10A), high Th (Table 3), and high incompatible element ratios (Th/Ce = 0.08–0.10, Th/Ta = 2.8–6.6, and La/Nb = 1.7–2.2). These characteristics are typical of continental crust (Taylor and McLennan, 1985; Rudnick and Fountain, 1995), and in sharp contrast to those for MORB and OIB (Sun and McDonough, 1989). Interestingly, these geochemical features are shown by all Group 1 samples, including the most primitive rocks (#Mg > 64), and suggest that mantle-derived melts were contaminated by crustal components prior

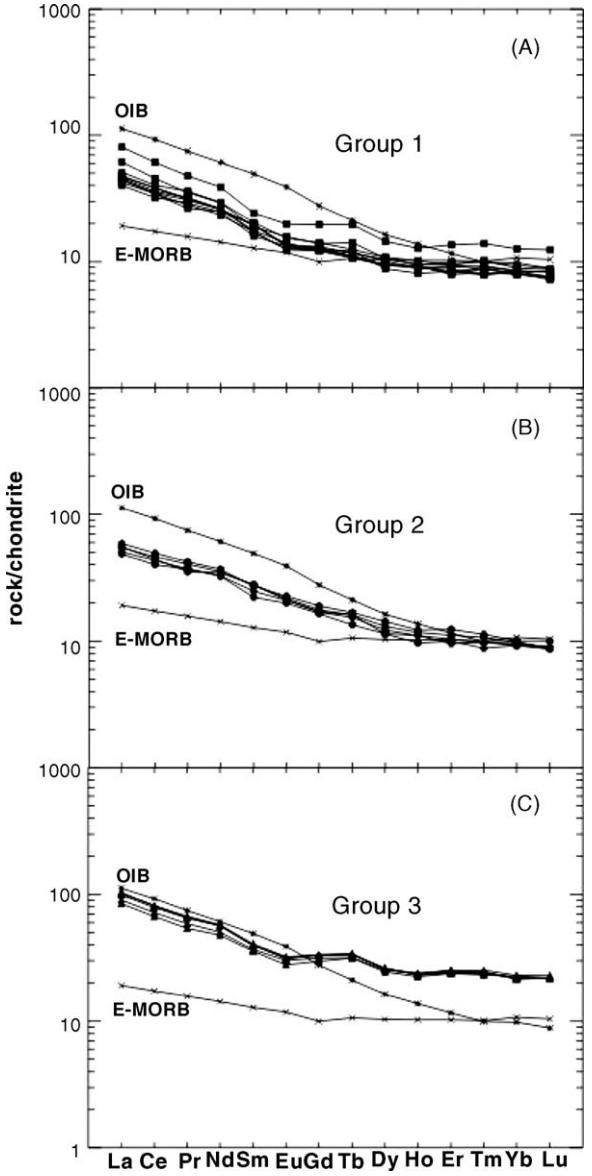


Fig. 11. Chondrite-normalized (Sun and McDonough, 1989) REE patterns for dolerites.

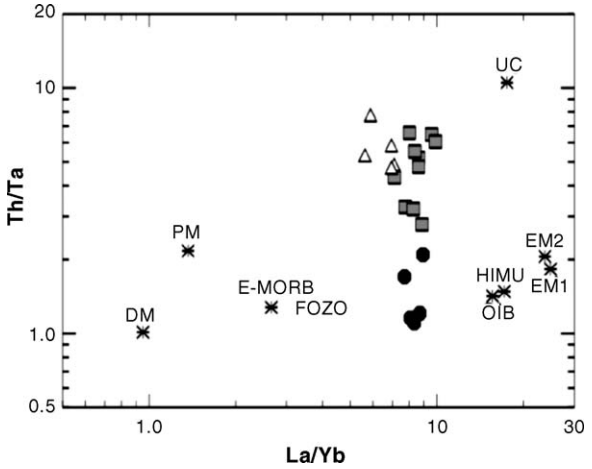


Fig. 12. Th/Ta–La/Yb diagram for dolerites. DM, depleted mantle; PM, primitive mantle; UC, upper continental crust; HIMU, high U/Pb mantle source; EM1 and EM2, enriched mantle sources; FOZO, lower mantle plume component; EMORB, enriched MORB. References are cited in Condie (1997). Symbols as in Fig. 5.

to sill emplacement. Th/Ta and La/Yb ratios constrain the sources and evolution of mafic melts, because they are invariants during fractional differentiation (Condie, 1997). The absence of significant variations in Th/Ce and La/Nb ratios (Bingen and Demaiffe, 1999) is also evidence for crustal contamination prior to (not during) sill emplacement. The absence of a trend in the Th/Ta–La/Yb diagram (Fig. 12), however, argues against contamination of original magma by crustal material during emplacement. We conclude that Nb–Ta depletion of primary melts for Group 1 sills was probably caused by contamination of mantle-derived melts by crustal components prior to sill emplacement, possibly above a Neoproterozoic mantle plume. Group 1 sill analyses and those of NNW-trending dykes of the Sharyzhalgai massif (Sklyarov et al., 2003) both plot in the basalt field in a total alkalis versus $SiO_2$ plot. Trace-element and REE spidergrams, as well as the trends of $TiO_2$, Ni, Y, and Nb versus Mg# are also similar for intrusions from the two areas, suggesting that they could be related in origin.

Despite a small Nb anomaly in spidergrams (Fig. 10B) it is unlikely that Group 2 dykes were contaminated significantly by crustal material. Incompatible element ratios (Th/Ce = 0.04–0.05, Th/Ta = 1.11–2.09) are similar to those typical of mantle-derived melts (Th/Ce is 0.04 in E-MORB and 0.05 in OIB; Th/Ta is 1.3 in E-MORB and 1.5 in OIB; Sun and McDonough, 1989). In addition, high Ti/Yb ratios (5000–6000) in Group 2 dykes suggest that crustal contamination was not significant (Leeman and Hawkesworth, 1986; Hart et al., 1989).

Two alternative processes could explain the negative Nb anomaly observed in Group 2 dykes: (1) subduction-related enrichment of lithospheric mantle (Kepezhinkas et al., 1997) and (2) chemical interaction between lithospheric mantle and asthenosphere-derived magmas having incompatible elements but little Nb (Arndt and Christensen, 1992; Patchett et al., 1994). Normalized Ta/La ratios are significantly higher than those for a mantle source metasomatised by subduction-related processes (Fig. 13) (Wang et al., 2004). Lower

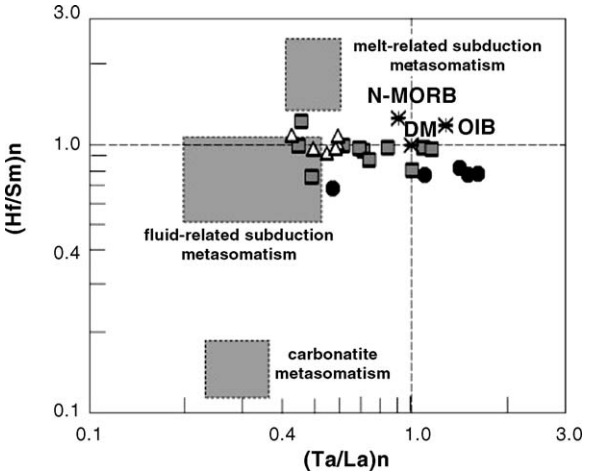


Fig. 13. Discrimination of magma sources using the $(Hf/Sm)_n$–$(Ta/La)_n$ diagram of Wang et al. (2004). Symbols as in Fig. 5.

La/Nb (1.2–1.4) and La/Ta (10–22) for Group 2 dykes also argue against subduction-related enrichment of a lithospheric source and confirm the presence of asthenosphere-derived magma in the original source (Fitton et al., 1988; Leat et al., 1988; Thompson and Morrison, 1988). Accordingly, we suggest that the second possibility can best explain the negative Nb anomalies in Group 2 dykes. In this model, interaction between asthenosphere-derived magma with lithospheric mantle leads to negative Nb anomalies, because oxide minerals (spinel, ilmenite, rutile), as the main carriers of Nb, dissolve in magmas much more slowly than do mantle silicates, which add other incompatible elements to the source. For Group 2 dolerite, we propose spinel as a good candidate for the oxide phase, rather than ilmenite or rutile, because the Nb anomalies are not accompanied by negative Ti anomalies (Fig. 10B). Negative P anomalies in Group 2 dykes can be explained by apatite fractionation.

Rock compositions and sub-parallel trends in spidergrams (Fig. 10B) imply that Group 2 rocks were formed by differentiation of magma from a single source. Group 2 dolerite analyses plot between E-MORB-FOZO and HIMU-EM-OIB sources in the Th/Ta versus La/Yb diagram (Fig. 12), suggesting that the parent magma originated from either a plume-related source or an asthenospheric-lithospheric source. Because Group 2 dykes are not widespread within the study area (less than 1% of bedrock), we consider a plume source to be less likely. Passive asthenospheric upwelling and decompression during lithospheric stretching (e.g. McKenzie and Bickle, 1988; Arndt and Christensen, 1992; Patchett et al., 1994) can explain the chemical characteristics and inferred low magma volumes for Group 2 dykes.

All Group 3 dyke samples, including the least differentiated rocks, with Mg# ~48, exhibit a pronounced negative Nb–Ta anomaly (Fig. 10C). Group 3 dykes also have high $Fe_2O_3t$ (>15%) and $TiO_2$ (2.2–3.1%), unlike melts that have been significantly contaminated by continental crust (Patchett et al., 1994). However, high Th/Ta ratios (2.23–5.32), close to those of continental crust (Rudnick and Fountain, 1995), and the occurrence of inherited zircons in sample 03201, suggest that some crustal contamination did occur. Possible explanations for negative Nb–Ta anomalies for melts that did not undergo significant crustal contamination were discussed above in relation to Group 2 dykes. We consider subduction-related enrichment of lithospheric mantle (Kepezhinkas et al., 1997) to be the most likely model for the origin of Group 3 dykes.

Group 3 dykes have $(Ta/La)_n = 0.42–0.68$ and $(Hf/Sm)_n = 0.73–1.11$, and plot within the fluid-related subduction metasomatism field on the diagram (Fig. 13) of Wang et al. (2004). Furthermore, high La/Nb (1.7–2.7) and La/Ta (25–40) argue in favour of a lithospheric mantle source altered by subduction-related fluids (Fitton et al., 1988; Leat et al., 1988; Thompson and Morrison, 1988). Group 3 samples (Fig. 11C) have the highest REE contents, relatively flat REE abundance patterns, gently sloping HREE fields, and high Y abundances (Table 4). These characteristics can be explained by the absence of a garnet component in the mantle source. Hanski and Smolkin (1995) showed that melting of garnet-free refractory mantle residue can generate high-$Fe_2O_3t$ rocks enriched in $TiO_2$, HFSE, and LREE, because this source may have relatively high $Fe_2O_3t$ which will increase during melting due to its moderately incompatible behaviour (Hirose and Kushiro, 1993; Wang et al., 2004). Moreover, this model suggests that the magma should be enriched by LREE and other incompatible elements prior to emplacement (Hanski and Smolkin, 1995). We consider this model to be a plausible explanation for genesis of Group 3 dykes.

### 5.3. *Neoproterozoic reconstruction of Siberia and Laurentia*

Numerous models have been proposed recently for the position of Siberia in the Meso-to Neoproterozoic supercontinent Rodinia (see Pisarevsky and Natapov, 2003, for a review). Most juxtapose Siberia, in various orientations, against the northern margin of Laurentia (e.g. Hoffman, 1991; Condie and Rosen, 1994; Frost et al., 1998; Rainbird et al., 1998; Ernst et al., 2000). Although the apparent absence of Mackenzie or Franklin magmatic equivalents in Siberia has been

used as an argument against these reconstructions (e.g. Shellnutt et al., 2004), our new results, together with those of Sklyarov et al. (2003), show that mafic intrusions broadly similar in age to the Franklin magmatic event in Laurentia exist along the southwestern margin of Siberia. Within their assigned uncertainties, however, the Ar–Ar ages of 741 ± 4 Ma for Group 1 sills and 758 ± 4 Ma for dykes in the Sharyzhalgai massif indicate that these intrusions are significantly older than the Franklin event (723 + 4/−2 Ma, U–Pb baddeleyite, Heaman et al., 1992). Nevertheless, the Ar–Ar ages are probably less robust than the Franklin U–Pb age, and U–Pb geochronology of the Siberian intrusions would facilitate a more meaningful comparison.

Shellnutt et al. (2004, their Fig. 9) showed that variations of CaO, MgO, and Zr versus $SiO_2$ for the Coronation sills are similar to those observed in regional average analyses of Franklin intrusions. Variations of CaO and Zr with $SiO_2$ for Group 1 sills of the Biryusa block (Table 3) also plot within the range of the Franklin results, and the field of MgO versus $SiO_2$ for Group 1 sills overlaps the corresponding field for the Franklin intrusions. These results provide only weak support for a genetic relation between the Group 1 sills of Siberia and the Franklin intrusions of Laurentia. More detailed geochemical comparisons between the Biryusa and Franklin intrusions are less diagnostic, owing to their strong dependence on crustal thickness, upper mantle heterogeneity, and other factors, most of which are highly variable even within a single region.

Our geochronology indicates that sedimentary rocks of the middle Karagas Group were deposited at ∼740 Ma, and the upper Karagas Group between 740 and 612 Ma. Sklyarov et al. (2001) also suggested a Neoproterozoic age for the Karagas Group. In northern Laurentia, Frisch and Trettin (1991) proposed an Early Cambrian age for the lowermost passive margin sediments of the Kennedy Channel and Ella Bay Formations of northern Greenland and Ellesmere Island. Dewing et al. (2004), however, revisited the Laurentian succession and proposed a Late Neoproterozoic age. Rainbird and de Freitas (1997) suggested that the 723 Ma Franklin event marks the initiation of rifting in northern Laurentia. Passive margin sedimentation along northern Laurentia, therefore, may be significantly younger than deposition of the lower and middle Karagas Group, but could be coeval with the upper Karagas or the Oselkovaya Groups.

Although there are no paleomagnetic data for Siberia at 740 Ma, matching of ∼1050–980 Ma apparent polar wander (APW) paths (Pisarevsky and Natapov, 2003), locates Siberia some distance to the northwest of Laurentia (present coordinates), and refutes previous reconstructions that place Siberia directly adjacent to either northern or western Laurentia (e.g. Hoffman, 1991; Sears and Price, 2003). Within the uncertainties of the paleomagnetic data (Table 1 of Pisarevsky and Natapov, 2003), however, this reconstruction can be modified to allow southwestern Siberia to occupy a position closer to northern Laurentia. In this reconstruction (Fig. 14), and assuming that the Franklin magmatic province had roughly radial symmetry and extended as far to the north of Laurentia as it does within the continent, the 740 Ma sills and dykes of Siberia could be related to the Franklin plume of Laurentia. Similarly, it is possible that equivalents of the 1267 Ma Mackenzie dyke swarm (Fahrig, 1987; Schwab et al., 2004) also occur in southern Siberia, although evidence has yet to be found. The space between Siberia and Laurentia leaves room for other crustal blocks (e.g. northern Alaska, Chukchi Peninsula, and others) that were juxtaposed against northern Laurentia prior to the ∼125 Ma opening of the Canada basin (e.g. Zonenshain et al., 1990; Embry, 1998; Natal'in, 2004; Drachev, 2004). Another possibility is that the region between Siberia and Laurentia was occupied, at 723 Ma, by a large oceanic igneous province, similar in scale to the present Ontong-Java plateau, such as has been proposed for the space between Kalahari and Laurentia at 1100 Ma (Hanson et al., 2004).

The relative motions of Siberia and Laurentia after ∼740 Ma are not clear owing to the lack of reliable Late Neoproterozoic paleomagnetic data from the two cratons (Pisarevsky, 2005). Nevertheless, our new geochemical and geochronological data put some constraints on the southwest Siberian margin following breakup. The 612 Ma north-trending Group 2 dykes may have formed above an asthenospheric upwelling adjacent to the Siberian margin. The occurrence of ∼630 Ma carbonatites and alkaline ultramafic rocks in the Sharyzhalgai massif (Yarmolyuk and Kovalenko, 2001) supports this suggestion.

The 511 Ma age for northwest-trending Group 3 dykes corresponds to the time of closure of the Paleo-Asian Ocean along the southern Siberian margin and formation of the Central Asian Orogenic Belt (Dobretsov et al., 2003). Numerous terranes were accreted to the Siberian margin during this orogeny. Peak high-grade metamorphism occurred at ∼500 Ma (Donskaya et al., 2000, and references therein). Examples of syn- and post-orogenic extensional tectonics (e.g. Fossen, 2000) and post-collisional mafic magmatism (e.g. Aït-Djafer et al., 2003) are known. Such a situation is possible in the case of delamination of an accreted plate and its thrusting onto and beneath a wedge-shaped cratonic margin ('wedge tectonics', Snyder, 2002, and references therein). A

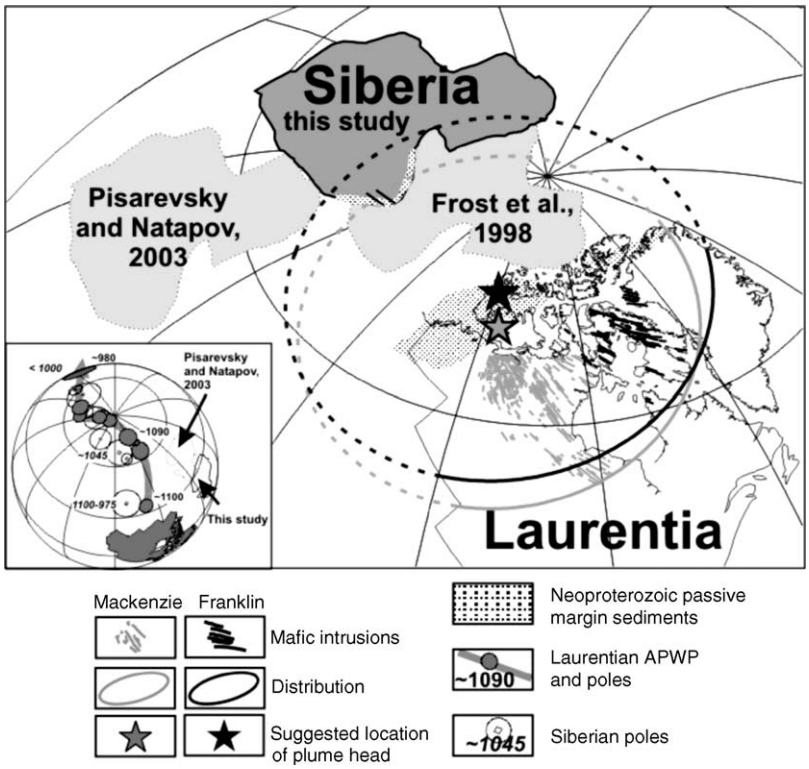


Fig. 14. A modified Siberia-Laurentia reconstruction that satisfies paleomagnetic data and permits a closer fit of the continents. Siberia is rotated −165.4° (clockwise) to Laurentia (in present coordinates) about an Euler pole at 68.6°N, 118.5°E. Rotation parameters for two other reconstructions shown are listed in Pisarevsky and Natapov (2003). Greenland is rotated to Laurentia with Euler parameters (latitude [°N], longitude [°E], rotation [°]) of (67.5, 241.5, −13.8). Northern Ellesmere Island is rotated to Laurentia (67.0, 260, −12.0). Inset shows Laurentian and Siberian palaeopoles for ∼1100–980 Ma (Table 1 in Pisarevsky and Natapov, 2003).

deep seismic profile across the southern Siberian margin (Fig. 11 in Zorin et al., 2002) shows structures compatible with this scenario, but their ages are not well known. Dykes similar in composition (enriched in HFSE and REE) to Group 3 dykes occur in the Sharyzhalgai massif and in other areas along the southwest Siberian margin (Gladkochub et al., 2003), although their ages are uncertain. If they are also Early Paleozoic, similar tectonic environments (wedge tectonics) may have been prevalent in this region during formation of the Central Asian Orogenic Belt.

### *5.4. Possible connections between Siberia and Australia*

Dated at 741 and 511 Ma, mafic intrusions of Groups 1 and 3 in southwestern Siberia are similar in age to two significant mafic units in Australia: the 755 ± 3 Ma Mundine Well dyke swarm, which extends for ∼900 km along the northwestern margin of Australia (Wingate and Giddings, 2000), and the ∼510 Ma Kalkarinji LIP, which probably extended across much of northern and central Australia (Hanley and Wingate, 2000; Glass, 2002; Macdonald et al., 2005). A high-quality paleopole for the Mundine Well dykes indicates that Australia occupied low latitudes and was in almost its present orientation at 755 Ma (Wingate and Giddings, 2000). Unfortunately, there are no paleomagnetic data of this age from Siberia to which the Australian result can be compared. There are published reconstructions, however, which are not supported by paleomagnetic data, and in which northern Australia is juxtaposed against southern Siberia (e.g. Hoffman, 1991; Sears and Price, 2003). In each of these reconstructions, the distance between the Biryusa intrusions in Siberia and the Mundine Well dykes in Australia is >5000 km, which would make any genetic relation between them highly improbable.

Australia is represented by a single paleopole at 1070 Ma, and there is no APW path for Australia that can be compared to those for Siberia or Laurentia, hence the Late Mesoproterozoic paleolongitude of Australia is unconstrained. Within the limits of uncertainty in matching the Laurentian and Siberian APW paths, and depending on the extent of the Mawson block beneath

Antarctic ice (Collins and Pisarevsky, 2005), the paleolatitude of Australia at 1070 Ma is compatible with the intriguing possibility that the Australia-Mawson continent occupied the intervening space between northern Laurentia and southern Siberia. Note that this idea is largely speculative, and remains to be tested against additional paleomagnetic and geological data. In this scenario, equivalents of the Franklin and Mackenzie intrusions might be expected to occur in Antarctica, and equivalents of the Siberian intrusions in northern Australia. The Mundine Well dykes, in the Pilbara region of Australia, remain unlikely equivalents of Group 1 sills, however, because they are located >2000 km from the northern (New Guinea) margin of Australian continental crust, where no rocks of this age have been identified (although Proterozoic basement is inferred, e.g. Baldwin and Ireland, 1995).

Li et al. (submitted for publication) presented new geochemical data for the Mundine Well dykes and inferred that they were most likely derived from an OIB-type asthenospheric mantle source, with variable degrees of crustal contamination during magma ascent and emplacement. They suggested that the Mundine Well dykes, together with coeval intrusions in South China and the Seychelles, could have been generated by melting within a vast asthenospheric mantle superplume that developed beneath, and led to breakup of, the Rodinia supercontinent (Li et al., 2003). In such a scenario, it is possible that the mafic magmatic event during which Group 1 sills were emplaced was part of this widespread activity.

Despite the close agreement of isotopic ages for 511 Ma Group 3 dykes and the ~510 Ma Kalkarinji LIP, reliable paleomagnetic data do not permit a Cambrian connection between Australia and Siberia. At this time, Siberia was an isolated continent situated in low to intermediate southern latitudes, whereas Australia was located in equatorial latitudes, north of Siberia, with its southern margin attached to Antarctica and the rest of Gondwanaland (Smethurst et al., 1998; Li and Powell, 2001; McElhinny et al., 2003).

## Acknowledgements

The authors are grateful to Richard Ernst and an anonymous reviewer for valuable comments that significantly improved the manuscript. This research was supported in part by grants from the Russian Foundation for Basic Research (04-05-64159, 04-05-64412), Russian Science Support Foundation, and the Russian Ministry of Education (768.2003.5). U–Pb analyses were conducted using the SHRIMP II ion microprobe in Perth, Australia, which is operated by a university–government consortium, with the support of the Australian Research Council. This is Tectonics Special Research Centre publication number XXX.

## References

Aït-Djafer, S., Ouzegane, K., Liégeois, J.-P., Kienast, J.R., 2003. An example of postcollisional mafic magmatism: the gabbro–anorthosite layered complex from the Tin Zebane area (western Hoggar, Algeria). J. Afr. Earth Sci. 37, 313–330.

Arndt, N.T., Christensen, U., 1992. The role of lithospheric mantle in continental flood volcanism: thermal and geochemical constraints. J. Geophys. Res. 97, 10967–10981.

Baldwin, S.L., Ireland, T.R., 1995. A tale of two eras: Pliocene-Pleistocene unroofing of Cenozoic and late Archean zircons from active metamorphic core complexes, Solomon Sea, Papua New Guinea. Geology 23, 1023–1026.

Bingen, B., Demaiffe, D., 1999. Geochemical signature of the Egersund basaltic dyke swarm, SW Norway, in the context of late-Neoproterozoic opening of the Iapetus Ocean. Norsk Geologisk Tidsskrift 79, 69–86.

Claoué-Long, J.C., Compston, W., Roberts, J., Fanning, C.M., 1995. Two Carboniferous ages: a comparison of SHRIMP zircon ages with conventional zircon ages and 40Ar/39Ar analysis. In: Berggren, W.A., Kent, D.V., Aubrey, M.-P., Hardenbol, J. (Eds.), Geochronology, Time Scales, and Global Stratigraphic Correlation, pp. 3–21 (S.E.P.M. Special Publ. 54).

Collins, A.C., Pisarevsky, S.A., 2005. Amalgamating eastern Gondwana: the evolution of the Circum-Indian Orogens. Earth-Sci. Rev. 71, 229–270.

Condie, K.C., 1997. Sources of Proterozoic mafic dyke swarms: constraints from Th/Ta and La/Yb ratios. Precamb. Res. 81, 3–14.

Condie, K.C., Rosen, O.M., 1994. Laurentia–Siberia connection revisited. Geology 22, 168–170.

Dalrymple, G.B., Lanphere, M.A., 1971. $^{39}Ar/^{40}Ar$ technique of K/Ar dating: a comparison with the conventional technique. Earth Planet. Sci. Lett. 12, 300–308.

Dewing, K., Harrison, J.C., Pratt, B.R., Mayr, U., 2004. A probable late Neoproterozoic age for the Kennedy Channel and Ella Bay formations, northeastern Ellesmere Island and its implications for passive margin history of the Canadian Arctic. Can. J. Earth Sci. 41, 1013–1025.

Dobretsov, N.L., Buslov, M.M., Vernikovsky, V.A., 2003. Neoproterozoic to Early Ordovician evolution of the Paleo-Asian Ocean: implications to the breakup of Rodinia. Gondwana Res. 6, 143–159.

Domyshev, V.G., 1976. Riphean basites of the Baikal-Sayan-Yenisei margin of the Siberian platform. Nauka, Novosibirsk (in Russian).

Donskaya, T.V., Sklyarov, E.V., Gladkochub, D.P., Mazukabzov, A.M., Sal'nikova, E.B., Kovach, V.P., Yakovleva, S.Z., Berezhnaya, N.G., 2000. The Baikal collisional metamorphic belt. Doklady Earth Sci. 374, 1075–1079.

Drachev, S.S., 2004. Siberian Arctic continental margin: constraints and uncertainties of plate tectonic model. AGU Fall Meet, Supplement (Abstract GP43C-07).

Embry, A.F., 1998. Counterclockwise rotation of the Arctic Alaska plate: best available model or untenable hypothesis for the opening of the Amerasia Basin. Polarforschung 68, 247–255.

Ernst, R.E., Buchan, K.L., 2001. Large mafic magmatic events through time and links to mantle-plume heads. In: Ernst, R.E., Buchan, K.L. (Eds.), Mantle Plumes: Their 15 Identification Through Time.

Boulder, Colorado. Geological Survey of America Special Paper 352, pp. 483–575.

Ernst, R.E., Buchan, K.L., Hamilton, M.A., Okruign, A.V., Tomshin, M.D., 2000. Integrated paleomagnetism and U–Pb geochronology of mafic dykes of eastern Anabar Shield region, Siberia: Implications for Mesoproterozoic paleolatitude of Siberia and comparison with Laurentia. J. Geol. 108, 381–401.

Fahrig, W.F., 1987. The tectonic settings of continental mafic dyke swarms: failed arm and early passive margin. In: Halls, H.C., Fahrig, W.F. (Eds.), Mafic Dyke Swarms. Geol. Assoc. Can., Special Paper 34, pp. 331–348.

Fitton, J.G., James, D., Kempton, P.D., Ormerod, D.S., Leeman, W.P., 1988. The role of lithospheric mantle in the generation of late Cenozoic basic magmas in the western United States. In: Cox, K.G., Menzies, M.A. (Eds.), Oceanic and continental lithosphere: similarities and differences. J. Petrology, pp. 331–349 (special volume).

Fleash, R.J., Sutter, J.F., Elliot, D.H., 1977. Interpretation of discordant $^{39}Ar/^{40}Ar$ age spectra of Mesozoic tholeiites of Antarctica. Geochim. Cosmochim. Acta 41, 15–32.

Fossen, H., 2000. Extensional tectonics in the Caledonides: synorogenic or postorogenic? Tectonics 19, 213–224.

Frisch, T., Trettin, H.P., 1991. Precambrian successions in the northernmost part of the Canadian Shield. In: Trettin, H.P. (Ed.), Geology of the Innuitian Orogen and Arctic Platform of Canada and Greenland, vol. 3. Geol. Surv. Can., Geology of Canada, pp. 103–108.

Frost, B.R., Avchenko, O.V., Chamberlain, K.R., Frost, C.D., 1998. Evidence for extensive Proterozoic remobilization of the Aldan Shield and implications for Proterozoic plate tectonic reconstructions of Siberia and Laurentia. Precamb. Res. 89, 1–23.

Garbe-Schonberg, C.-D., 1993. Simultaneous determination of thirty-seven trace elements in twenty-eight international rock standards by ICP-MS. Geostand. Newsl. 17, 81–97.

Gladkochub, D.P., Donskaya, T.V., Mazukabzov, A.M., Ponomarchuk, V.A., 2003. Alkaline porphyrite as an indicators of Early Paleozoic collision events within southern margin of the Siberian craton. In: Polyakov, G.V. (Ed.), Recent problems of petrology and metallogeny of igneous rocks. GEO Publisher, Novosibirsk, pp. 6–7 (in Russian).

Glass, L.M., 2002. Petrogenesis and geochronology of the low-Ti Kalkarinji continental flood basalt province. Ph.D. Thesis, Australian National University, Canberra, 326 p.

Hanley, L.M., Wingate, M.T.D., 2000. A SHRIMP zircon age for an Early Cambrian dolerite dyke-an intrusive phase of the Antrim Plateau Volcanics of northern Australia. Aust. J. Earth Sci. 46, 1029–1040.

Hanski, E.J., Smolkin, V.F., 1995. Iron- and LREE-enriched mantle source for early Proterozoic intraplate magmatism as exemplified by the Pechenga ferropicrites, Kola Peninsula Russia. Lithos 34, 107–125.

Hanson, R.E., Bowring, S.A., Ramezani, J., Dalziel, I.W.D., Crowley, J.L., Gose, W.A., Pancake, J.A., Seidel, E.K., Blenkinsop, T.G., Mukwakwami, J., 2004. 1.1-Billion-year-old large-scale magmatism in the Kalahari and Laurentian cratons during Rodinia supercontinent assembly. Science 304, 1126–1129.

Harlan, S.S., Heaman, L., LeCheminant, A.N., Premo, W.R., 2003. Gunbarrel mafic magmatic event: a key 780 Ma time marker for Rodinia plate reconstructions. Geology 31, 1053–1056.

Hart, W.K., Wolde, G., Walter, R.C., Mertzman, S.A., 1989. Basaltic volcanism in Ethiopia: constraints on continental rifting and mantle interactions. J. Geophys. Res. 94, 7731–7748.

Heaman, L.M., LeCheminant, A.N., Rainbird, R.H., 1992. Nature and timing of Franklin igneous events, Canada: Implications for a Late Proterozoic mantle plume and the breakup of Laurentia. Earth Planet. Sci. Lett. 109, 117–131.

Hirose, K., Kushiro, I., 1993. Partial melting of dry peridotites at high pressures: Determination of compositions of melts segregated from peridotite using aggregates of diamond. Earth Planet. Sci. Lett. 114, 477–489.

Hoffman, P.F., 1991. Did the breakout of Laurentia turn Gondwana inside out? Science 252, 1409–1412.

Jensen L.S., 1976. A new cation plot for classifying subalkalic volcanic rocks. Ontario Department of Mines, Miscellaneous Paper 66.

Kepezhinkas, P., McDermott, F., Defant, M.J., Hochstaedter, A., Drummond, M.S., Hawkesworth, C.J., Koloskov, A., Maury, R.C., Bellon, H., 1997. Trace element and Sr–Nd–Pb isotopic constraints on a three-component model of Kamchatka Arc petrogenesis. Geochim. Cosmochim. Acta 61, 577–600.

Kheraskova, T.N., Didenko, A.N., Bush, V.A., Volozh, Y.A., 2003. The Vendian–Early Paleozoic history of the continental margin of eastern Paleogondwana, Paleoasian Ocean, and Central Asian foldbelt. Russian J. Earth Sci. 5, 165–184.

Khomentovsky, V.V., 1990. The Vendian of Siberian platform. In: Sokolov, B.S., Iwanowski, A.B. (Eds.), The Vendian system. Springer-Verlag, Berlin, New York, pp. 83–160.

Khomentovsky, V.V., 2002. Baikalian of Siberia (850–650 Ma). Russian Geology and Geophysics 43, 313–333.

Leat, P.T., Thompson, R.N., Morrison, M.A., Hendry, G.L., Dickin, A.P., 1988. Compositionally-diverse Miocene-Recent rift-related magmatism in northwest Colorado: partial melting, and mixing of mafic magmas from 3 different asthenospheric and lithospheric mantle sources. In: Cox, K.G., Menzies, M.A. (Eds.), Oceanic and continental lithosphere: similarities and differences. J. Petrology, pp. 351–377 (special volume).

Leeman, W.P., Hawkesworth, C.J., 1986. Open magma systems: trace elements and isotopic constraints. J. Geophys. Res. 91, 5901–5912.

Levitskii, V.I., Mel'nikov, A.I., Reznitskii, L.Z., Bibikova, E.V., Kirnozova, T.I., Kozakov, I.K., Makarov, V.A., Plotkina, Yu.V., 2002. Early Proterozoic postcollisional granitoids in southwestern Siberian craton. Russian Geol. Geophys. 43, 717–731.

Li, Z.X., Li, X.H., Kinny, P.D., Wang, J., Zhang, S., Zhou, H., 2003. Geochronology of Neoproterozoic syn-rift magmatism in the Yangtze Craton, South China and correlations with other continents: evidence for a mantle superplume that broke up Rodinia. Precamb. Res. 122, 85–109.

Li, X.H., Li, Z.X., Wingate, M.T.D., Chung, S.L., Liu, Y., Lin, G.C., Li, W.X. Geochemistry of the 755 Ma Mundine Well dyke swarm, northwestern Australia: part of a Neoproterozoic mantle superplume beneath Rodinia? Precamb. Res., submitted for publication.

Li, Z.-X., Powell, C.McA., 2001. An outline of the palaeogeographic evolution of the Australasian region since the beginning of the Neoproterozoic. Earth-Sci. Rev. 53, 237–277.

Macdonald, F.A., Wingate, M.T.D., Mitchell, K., 2005. Geology and age of the Glikson impact structure, Western Australia. Aust. J. Earth Sci. 52 (4/5), 641–651.

McElhinny, M.W., Powell, C.McA., Pisarevsky, S.A., 2003. Paleozoic terranes of Eastern Australia and the drift history of Gondwana. Tectonophysics 362, 41–65.

McKenzie, D., Bickle, M.J., 1988. The volume and composition of melt generated by extension of the lithosphere. J. Petrology 29, 625–679.

Natal'in, B.A., 2004. Phanerozoic tectonic evolution of the Chukotka-Arctic block: problems of the rotational model. In: AGU Fall Meet Supplement, (Abstract GP43C-04).

Patchett, P.J., Lehnert, K., Rehkämper, M., Sieber, G., 1994. Mantle and crustal effect on the geochemistry of Proterozoic dikes and sills in Sweden. J. Petrology 35, 1095–1125.

Pisarevsky, S.A., 2005. New edition of the Global Paleomagnetic Database. EOS Trans. 86 (17), 170.

Pisarevsky, S.A., Natapov, L.M., 2003. Siberia and Rodinia. Tectonophysics 375, 221–245.

Pisarevsky, S.A., Komissarova, R.A., Khramov, A.N., 2000. New palaeomagnetic results from Vendian red sediments in Cisbaikalia and the problem of the relationship of Siberia and Laurentia in the Vendian. Geophys. J. Int. 140, 598–610.

Pisarevsky, S.A., Wingate, M.T.D., Powell, C.McA., Johnson, S., Evans, D.A.D., 2003. Models of Rodinia assembly and fragmentation. In: Yoshida, M., Windley, B., Dasgupta, S. (Eds.), Proterozoic East Gondwana: supercontinent assembly and breakup, vol. 206. Geological Society of London Special Publication, pp. 35–55.

Rainbird, R.H., de Freitas, T.A., 1997. Stratigraphic evidence for the Siberia-Laurentia connection and Early Cambrian rifting: comment. Geology 25, 569–570.

Rainbird, R.H., Stern, R.A., Khudoley, A.K., Kropachev, A.P., Heaman, L.M., Sukhorukov, V.I., 1998. U–Pb geochronology of Riphean sandstone and gabbro from southeast Siberia and its bearing on the Laurentia-Siberia connection. Earth Planet. Sci. Lett. 164, 409–420.

Rudnick, R.L., Fountain, D.M., 1995. Nature and composition of the continental crust: a lower crustal perspective. Rev. Geophys. 33, 267–309.

Schwab, D.L., Thorkelson, D.J., Mortensen, J.K., Creaser, R.A., Abbott, J.G., 2004. The Bear River dykes (1265–1269 Ma): westward continuation of the Mackenzie dyke swarm into Yukon, Canada. Precamb. Res. 133, 175–186.

Sears, J.W., Price, R.A., 2003. Tightening the Siberian connection to western Laurentia. Geol. Soc. Am. Bull. 115, 943–953.

Sears, J.W., Price, R.A., Khudoley, A.K., 2004. Linking the Mesoproterozoic Belt-Purcell and Udzha basins across the west Laurentia-Siberia connection. Precamb. Res. 129, 291–308.

Shellnutt, J.G., Dostal, J., Keppie, J.D., 2004. Petrogenesis of the 723 Ma Coronation sills, Amundsen basin, Arctic Canada: implications for the break-up of Rodinia. Precamb. Res. 129, 309–324.

Sklyarov, E.V., Gladkochub, D.P., Mazukabzov, A.M., Stanevich, M.A., Donskaya, T.V., Konstantinov, K.M., Sinzov, A.V., 2001. Indicator complexes of supercontinent Rodinia break up. In: Geological Excursion Guide of Workshop Supercontinents and Geological Evolution of Precambrian. Institute of Earth Crust, Irkutsk (in Russian).

Sklyarov, E.V., Gladkochub, D.P., Mazukabzov, A.M., Menshagin, Y.V., Watanabe, T., Pisarevsky, S.A., 2003. Neoproterozoic mafic dike swarms of the Sharyzhalgai metamorphic massif (southern Siberian craton). Precamb. Res. 122, 359–376.

Smethurst, M.A., Khramov, A.N., Torsvik, T.H., 1998. The Neoproterozoic and Palaeozoic palaeomagnetic data for the Siberian Platform: from Rodinia to Pangea. Earth Sci. Rev. 43, 1–24.

Snyder, D.B., 2002. Lithospheric growth at margins of cratons. Tectonophysics 355, 7–22.

Sovetov, J.K., 2002. Vendian foreland basin of the Siberian cratonic margin: Paleopangean accretionary phases. Russian J. Earth Sci. 4, 363–387.

Sun, S., McDonough, W.F., 1989. Chemical and isotopic systematics of oceanic basalts: implications for mantle composition and processes. In: Saunders, A.D., Norry, M.J. (Eds.), Magmatism in the Oceanic Basins, 42. Geological Society of London, pp. 313–345 (Special Publication).

Taylor, S.R., McLennan, S.M., 1985. The Continental Crust: Its Composition and Evolution. Blackwell, Oxford Press.

Thompson, R.N., Morrison, M.A., 1988. Asthenospheric and lower-lithospheric mantle contributions to continental extension magmatism: an example from the British Tertiary Province. Chem. Geol. 68, 1–15.

Turkina, O.M., Bibikova, E.V., Nozhkin, A.D., 2003. Stages and Geodynamic Settings of Early Proterozoic Granite Formation on the Southwestern Margin of the Siberian Craton. Doklady Earth Sci. 388, 159–163.

Wang, Y., Fan, W., Zhang, Y., Guo, F., Zhang, H., Peng, T., 2004. Geochemical, $^{40}Ar/^{39}Ar$ geochronological and Sr-Nd isotopic constraints on the origin of Paleoproterozoic mafic dikes from the southern Taihang Mountains and implications for the ca. 1800 Ma event of the North China Craton. Precamb. Res. 135, 55–77.

Winchester, J.A., Floyd, P.A., 1977. Geochemical discrimination of different magma series and their differentiation products using immobile elements. Chem. Geol. 20, 325–343.

Wingate, M.T.D., Campbell, I.H., Compston, W., Gibson, G.M., 1998. Ion microprobe U–Pb ages for Neoproterozoic basaltic magmatism in south-central Australia and implications for the breakup of Rodinia. Precamb. Res. 87, 135–159.

Wingate, M.T.D., Giddings, J.W., 2000. Age and paleomagnetism of the Mundine Well dyke swarm, Western Australia: implications for an Australia-Laurentia connection at 755 Ma. Precamb. Res. 100, 335–357.

Wingate, M.T.D., Pirajno, F., Morris, P.A., 2004. The Warakurna large igneous province: a new Mesoproterozoic large igneous province in west-central Australia. Geology 32, 105–108.

Wood, D.A., 1980. The application of a Th-Hf-Ta diagram to problems of tectonomagmatic classification and to establishing the nature of crustal contamination of basaltic lavas of the British Tertiary volcanic province. Earth Planet. Sci. Lett. 50, 11–30.

Yarmolyuk, V.V., Kovalenko, V.I., 2001. Late Riphean breakup between Siberia and Laurentia: evidence from intraplate magmatism. Doklady Earth Sci. 379, 525–528.

Zonenshain, L.P., Kuzmin, M.I., Natapov, L.M., 1990. Geology of the USSR: a plate tectonic synthesis. Geodynamics series 21, AGU, Washington, DC.

Zorin, Y.A., Mordvinova, V.V., Turutanov, E.Kh., Belichenko, B.G., Artemyev, A.A., Kosarev, G.L., Gao, S.S., 2002. Low seismic velocity layers in the Earth's crust beneath Eastern Siberia (Russia) and Central Mongolia: receiver function data and their possible geological implication. Tectonophysics 359, 307–327.